The Astrophysical Journal, 904:107 (21pp), 2020 December 1 https://doi.org/10.3847/1538-4357/abbf59

Investigating the Effect of Galaxy Interactions on the Enhancement of Active Galactic Nuclei at $0.5 < z < 3.0$

Ekta A. Shah[1,25], Jeyhan S. Kartaltepe[1], Christina T. Magagnoli[1], Isabella G. Cox[1], Caleb T. Wetherell[1], Brittany N. Vanderhoof[1], Antonello Calabro[2], Nima Chartab[3], Christopher J. Conselice[4], Darren J. Croton[5], Jennifer Donley[6], Laura de Groot[7], Alexander de la Vega[8], Nimish P. Hathi[9], Olivier Ilbert[10], Hanae Inami[11], Dale D. Kocevski[12], Anton M. Koekemoer[9], Brian C. Lemaux[13], Kameswara Bharadwaj Mantha[14], Stefano Marchesi[15,16], Marie Martig[17], Daniel C. Masters[18], Elizabeth J. McGrath[12], Daniel H. McIntosh[14], Jorge Moreno[19], Hooshang Nayyeri[20], Belen Alcalde Pampliega[21], Mara Salvato[22], Gregory F. Snyder[9], Amber N. Straughn[23], Ezequiel Treister[24], and Madalyn E. Weston[14]

[1] School of Physics and Astronomy, Rochester Institute of Technology, 84 Lomb Memorial Drive, Rochester NY 14623, USA; eas7266@rit.edu
[2] INAF OAR, via Frascati 33, Monte Porzio Catone I-00078, Italy
[3] Department of Physics and Astronomy, University of California, Riverside, 900 University Ave, Riverside, CA 92521, USA
[4] Centre for Particle Theory and Astronomy, University of Nottingham, Nottingham NG7 2RD, UK
[5] Centre for Astrophysics & Supercomputing, Swinburne University of Technology, P.O. Box 218, Hawthorn, Victoria 3122, Australia
[6] Los Alamos National Laboratory, P.O. Box 1663, Los Alamos, NM 87545, USA
[7] Department of Physics, The College of Wooster, 1189 Beall Avenue, Wooster, OH 44691, USA
[8] Department of Physics and Astronomy, Johns Hopkins University, Baltimore, MD 21218, USA
[9] Space Telescope Science Institute, 3700 San Martin Dr., Baltimore, MD 21218, USA
[10] Aix Marseille Université, CNRS, LAM (Laboratoire d'Astrophysique de Marseille) UMR 7326, F-13388, Marseille, France
[11] Hiroshima Astrophysical Science Center, Hiroshima University, 1-3-1 Kagamiyama, Higashi-Hiroshima, Hiroshima 739-8526, Japan
[12] Department of Physics and Astronomy, Colby College, Waterville, ME 04961, USA
[13] Department of Physics & Astronomy, University of California, Davis, One Shields Ave., Davis, CA 95616, USA
[14] Department of Physics and Astronomy, University of Missouri-Kansas City, Kansas City, MO 64110, USA
[15] INAF - Osservatorio di Astrofisica e Scienza dello Spazio di Bologna, Via Piero Gobetti, 93/3, I-40129, Bologna, Italy
[16] Department of Physics and Astronomy, Clemson University, Kinard Lab of Physics, Clemson, SC 29634, USA
[17] Astrophysics Research Institute, Liverpool John Moores University, 146 Brownlow Hill, Liverpool L3 5RF, UK
[18] IPAC, California Institute of Technology, 1200 E. California Blvd, Pasadena, CA 91125, USA
[19] Department of Physics and Astronomy, Pomona College, 333 N. College Way, Claremont, CA 91711, USA
[20] Center for Cosmology, Department of Physics and Astronomy, 4129 Reines Hall, University of California, Irvine, CA 92697, USA
[21] Departamento de Física de la Tierra y Astrofísica, Facultad de CC Físicas, Universidad Complutense de Madrid E-2840 Madrid, Spain
[22] Max-Planck-Institut für extraterrestrische Physik (MPE), Giessenbachstrasse 1, D-85748 Garching bei München, Germany
[23] Astrophysics Science Division, NASA's Goddard Space Flight Center, Code 665, Greenbelt, MD 20771, USA
[24] Instituto de Astrofisica, Facultad de Fisica, Pontificia Universidad Catolica de Chile, Casilla 306, Santiago 22, Chile
Received 2020 May 29; revised 2020 October 2; accepted 2020 October 5; published 2020 November 25

Abstract

Galaxy interactions and mergers are thought to play an important role in the evolution of galaxies. Studies in the nearby universe show a higher fraction of active galactic nuclei (AGNs) in interacting and merging galaxies than in their isolated counterparts, indicating that such interactions are important contributors to black hole growth. To investigate the evolution of this role at higher redshifts, we have compiled the largest known sample of major spectroscopic galaxy pairs (2381 with $\Delta V < 5000\,\mathrm{km\,s^{-1}}$) at $0.5 < z < 3.0$ from observations in the COSMOS and CANDELS surveys. We identify X-ray and IR AGNs among this kinematic pair sample, a visually identified sample of mergers and interactions, and a mass-, redshift-, and environment-matched control sample for each in order to calculate AGN fractions and the level of AGN enhancement as a function of relative velocity, redshift, and X-ray luminosity. While we see a slight increase in AGN fraction with decreasing projected separation, overall, we find no significant enhancement relative to the control sample at any separation. In the closest projected separation bin (< 25 kpc, $\Delta V < 1000\,\mathrm{km\,s^{-1}}$), we find enhancements of a factor of $0.94^{+0.21}_{-0.16}$ and $1.00^{+0.58}_{-0.31}$ for X-ray and IR-selected AGNs, respectively. While we conclude that galaxy interactions do not significantly enhance AGN activity on average over $0.5 < z < 3.0$ at these separations, given the errors and the small sample size at the closest projected separations, our results would be consistent with the presence of low-level AGN enhancement.

Unified Astronomy Thesaurus concepts: Active galactic nuclei (16); Galaxy interactions (600); Galaxy mergers (608); Extragalactic astronomy (506); Galaxy pairs (610); Interacting galaxies (802); High-redshift galaxies (734)

1. Introduction

Galaxy interactions and mergers play a crucial role in the evolution of galaxies. Studies based on observations in the nearby universe show that galaxy interactions have strong effects on the properties of galaxies, such as their morphology (e.g., Lotz et al. 2008; Darg et al. 2010; Ellison et al. 2010), star formation rates (SFRs; e.g., Ellison et al. 2008, 2013b; Patton et al. 2013), and active galactic nuclei (AGNs) activity (e.g., Alonso et al. 2007; Woods & Geller 2007; Ellison et al. 2008; Rogers et al. 2009; Darg et al. 2010).

Empirical relations such as the $M_{\mathrm{BH}} - \sigma$ relation (Ferrarese & Merritt 2000; Gebhardt et al. 2000; McConnell et al. 2012) suggest that galaxies and their central supermassive black holes

[25] LSSTC DSFP Fellow.

(SMBHs) evolve together. Hence, understanding the link between AGNs/SMBHs and galaxy mergers is paramount to understanding the processes responsible for the co-evolution of galaxies and their SMBHs. There are two core questions related to the causal merger–AGN connection: (i) Do all galaxy mergers produce AGNs? and (ii) Are mergers the primary trigger of AGNs?

To answer the first question, studies compare the AGN activity of interacting and merging galaxies with isolated (non-interacting) galaxies. For low-redshift ($0.01 < z < 0.20$) major galaxy pairs (stellar mass ratio < 4) selected from the Sloan Digital Sky Survey (SDSS), Ellison et al. (2013a) find a clear trend of increasing AGN excess (ratio of AGN fraction in paired galaxies compared to a control sample of isolated galaxies) with decreasing projected separation (< 40 kpc). They measure the largest enhancement of $\sim$2.5 at the closest projected separation (< 10 kpc). Numerous studies using a similar approach in the nearby universe find significant AGN enhancement in merging and/or interacting galaxies (Alonso et al. 2007; Woods & Geller 2007; Ellison et al. 2011, 2019; Satyapal et al. 2014; Weston et al. 2017).

For the second question, studies compare the merger and/or interaction fraction of an AGN sample with that of galaxies without AGNs. More than 80% of quasars (high-luminosity AGNs) in the nearby universe show signs of a recent or ongoing merger (Sanders et al. 1988a, 1988b; Bennert et al. 2008; Urrutia et al. 2008). Similarly, Koss et al. (2010) find a higher fraction of disturbed galaxies (18% versus 1%) and close pairs within 30 kpc (24% versus 1%) in Swift/BAT hard X-ray moderate-luminosity AGNs compared to normal (inactive) galaxies at $z < 0.5$. However, Ellison et al. (2019) show that about 63% of optically selected AGN host galaxies from SDSS do not show visual signs of disturbance and they do not have a companion galaxy within a 30 kpc projected separation, suggesting that recent interactions and mergers are not the primary trigger of optical AGNs. They also show that almost 60% of mid-IR-selected AGNs show signs of disturbances; hence, interactions play a significant role in feeding AGNs and obscured AGNs are more likely to be triggered via mergers.

At high redshift, the merger–AGN connection is even more controversial. Using a sample of 562 spectroscopic galaxy pairs (mass ratio < 10 and $0.25 < z < 1.05$), Silverman et al. (2011) find a higher ($\times$1.9) AGN fraction in paired galaxies at projected separation less than 75 kpc compared to a control galaxy sample. Lackner et al. (2014) apply an automated method of identifying mergers by median-filtering of the high-resolution COSMOS Hubble Space Telescope (HST) images (Koekemoer et al. 2007) to distinguish two concentrated galaxy nuclei at small separations. They use this method to identify late-stage mergers at $0.25 < z < 1.0$ and use X-ray observations to identify AGNs. They find higher ($\times$2) X-ray-selected AGN activity in their late-stage merger sample compared to a mass- and redshift-matched control sample. Treister et al. (2012) find a luminosity dependence of the merger–AGN connection at all redshifts ($0 < z < 3$), showing that the merger fraction in AGNs increases from less than $\sim$25% for low to moderate-luminosity AGNs ($\sim$10% for all AGN) to $\sim$70%–80% for the highest luminosity AGNs ($L_{\rm bol} > 10^{46}$ erg s^{-1}). This higher merger fraction in high-luminosity AGNs is absent in other studies (e.g., Hewlett et al. 2017; Villforth et al. 2017). Most studies based on low- or intermediate-luminosity AGNs (e.g., Grogin et al. 2005; Schawinski et al. 2011; Kocevski et al. 2012) do not find a higher merger fraction in AGNs at high redshift compared to non-AGNs.

Schawinski et al. (2012) study heavily obscured quasars at $z \sim 2$ and find a very low merger fraction in these AGN hosts, concluding that most of them are disks and not mergers. However, Donley et al. (2018) show that about 75% of luminous, heavily obscured IR-only AGNs (not X-ray detected) in CANDELS/COSMOS are potentially late-stage major mergers. Kocevski et al. (2015) find that $\sim$22% of heavily obscured AGNs at $z \sim 1$ show signs of interaction or merger compared to unobscured AGNs ($\sim$8%). Hence, different types of AGNs might be triggered by different processes.

Part of this discrepancy could be due to the different methods used to identify galaxy merger and/or galaxy pair samples, corresponding control samples, and the identification of AGNs in galaxies. Most of the studies use one of two methods to identify mergers/interactions: (i) using morphological signs of disturbances such as tidal tails, double nuclei, and tidal bridges, and (ii) identifying close pairs based on either spectroscopic or photometric redshifts. The first method is challenging at high redshift, as observable merger signatures are difficult to identify because of their low surface brightness. The second method, however, can provide a larger and more complete sample of interacting galaxies. Furthermore, it also includes flybys that may not eventually merge but could still have an impact on fueling AGN activity. To identify and confirm interacting galaxy pairs, high spectroscopic completeness is required. One can use photometric redshifts to select pairs, but the relatively large uncertainties on photometric redshifts increase the likelihood of a given pair being a chance projection along the line of sight rather than being physically associated.

The discrepancy could also be due to the use of different methods to identify AGNs, such as the detection of broad emission lines, using X-ray (or radio) luminosity thresholds to identify X-ray (radio) AGNs, emission line flux ratios to distinguish AGN-dominated galaxies from star-formation-dominated galaxies, and IR broadband colors to identify galaxies with a strong power-law slope in the mid-infrared. Each of these methods traces different physical components of AGNs (such as the accretion disk, dusty torus, radio lobes, jets, emission line regions, etc.). The identification of AGNs is therefore not consistent among all these methods. It is possible that an AGN might be identifiable at different wavelengths at different stages of the merger process or the AGN duty cycle, which could lead to different selection techniques resulting in different AGN fractions.

Although most massive galaxies have an SMBH at their center, only a relatively small fraction of SMBHs are actively accreting. Simulations of gas-rich galaxy mergers in the local universe show these events can provide the torques necessary for reducing most of the angular momentum ($\sim$99%) of gas in the galaxy, funneling gas inflows toward the nuclear region ($\sim$1 kpc), ultimately triggering AGN activity at 1 pc scales (e.g., Barnes & Hernquist 1991; Mihos & Hernquist 1996; Di Matteo et al. 2008; Hopkins et al. 2009). However, the properties of these gas inflows (mass, size, shape, strength, etc.) and their propagation could be sensitive to the gas fraction and gas distribution in the galaxies.

The average gas fraction of galaxies changes significantly with redshift. At $z \sim 2$, the gas fraction in massive spiral galaxies can be $\sim$50%, compared to $\sim$10% at $z \sim 0$ (Daddi et al. 2010;

Tacconi et al. 2010; Scoville et al. 2014). Furthermore, the distribution of gas is very clumpy, and its average velocity dispersion is higher ($\sigma \sim 40\,\mathrm{km\,s^{-1}}$) in high-redshift galaxies compared to that ($\sigma \sim 10$ $\mathrm{km\,s^{-1}}$) in low-redshift galaxies (Stott et al. 2016). While the abundance of gas in high-redshift galaxies might make it easier to form gas inflows through interactions, the high turbulence and velocity dispersion throughout the galaxy might weaken the propagation of inflows. Results of some simulations show significantly weaker gas inflows in high-redshift galaxy mergers compared to low-redshift galaxy mergers (e.g., Di Matteo et al. 2008; Fensch et al. 2017). Hence, the efficiency of galaxy interactions in enhancing AGN activity may change substantially with redshift (McAlpine et al. 2020).

Observing the evidence for this effect requires deep multi-wavelength observations of a large sample of galaxy pairs and mergers over a wide redshift range. Using the multiwavelength observations and dedicated spectroscopic surveys in the CANDELS (Grogin et al. 2011; Koekemoer et al. 2011) and COSMOS (Scoville et al. 2007) fields, we generated the largest known sample of 2381 spectroscopic galaxy pairs with a relative line-of-sight velocity less than $5000\,\mathrm{km\,s^{-1}}$ undergoing major (stellar mass ratio of primary to secondary < 4) galaxy interactions at $0.5 < z < 3.0$. We also compiled a sample of mass-, redshift-, and environment-matched isolated control galaxies. We use X-ray and IR observations to identify AGNs and compare the AGN fraction in paired and control galaxies to estimate interaction-induced AGN enhancement in paired galaxies.

The layout of this paper is as follows. We describe the survey data used and our spectroscopic observations in Section 2. In Section 3, we discuss the methods used to generate our galaxy pairs, visually identified mergers, and control samples. In Section 4.1, we identify X-ray and IR-selected AGNs. We estimate the AGN fraction and present our results on AGN enhancement for the spectroscopic galaxy pairs and visually identified samples in Sections 4.2 and 4.3, respectively. We discuss our results in Section 5 and summarize in Section 6. Throughout this work, we use a standard ΛCDM cosmology with $H_0 = 70\,\mathrm{km\,s^{-1}}$ $\mathrm{Mpc^{-1}}$, $\Omega_\Lambda = 0.7$, and $\Omega_M = 0.3$. All magnitudes are given in the observed AB system and mass values of the galaxies correspond to their stellar masses unless stated otherwise.

2. Data

We use deep multiwavelength CANDELS (PIs: S. Faber and H. Ferguson; Grogin et al. 2011; Koekemoer et al. 2011) and COSMOS (Scoville et al. 2007) observations for this study. Due to the extensive multiwavelength photometric and spectroscopic observations available in these fields, they provide a statistically robust and complete sample of massive galaxies out to redshift ∼3, required for our study.

CANDELS is a Multi-cycle HST Treasury program spanning an area of ∼960 $\mathrm{arcmin^2}$. It consists of two types of surveys covering five different fields on the sky: (i) the CANDELS/Deep Survey, covering ∼125 $\mathrm{arcmin^2}$ within the Great Observatories Origins Deep Survey (GOODS; Giavalisco et al. 2004) North (GOODS-N) and South (GOODS-S) fields, and (ii) the CANDELS/Wide Survey covering portions of GOODS-N, GOODS-S, the Extended Groth Strip (EGS; Davis et al. 2007), the Cosmic Evolution Survey (COSMOS; Scoville et al. 2007), and the UKIDSS Ultra-Deep Survey (UDS; Lawrence et al. 2007). All of these five fields were observed using near-IR filters F160W and F125W on the HST/Wide-Field Camera 3 (WFC3) and F606W and F814W on HST/Advanced Camera for Surveys (ACS).

COSMOS is the largest (∼2 $\mathrm{deg^2}$) contiguous-area HST survey (Koekemoer et al. 2007; Scoville et al. 2007), with coverage in ACS/F814W and a wealth of multiwavelength observations across the spectrum. The large area of COSMOS enables statistical studies of large samples, and in particular, allows for detailed analysis of the surrounding environment of galaxies and its impact on their evolution. In addition to the CANDELS observations of a small portion of COSMOS mentioned above, we also make use of observations across the full field in our analysis.

2.1. Photometry and Derived Physical Quantities

The source catalogs in the CANDELS fields were generated using the source detection algorithm SOURCE EXTRACTOR (Bertin & Arnouts 1996) applied to the F160W (*H*-band) 1 1/3 orbit depth CANDELS mosaic image for each field. We use the observed-frame multiwavelength (UV to near-IR) photometric catalogs produced by Nayyeri et al. (2017), Guo et al. (2013), Barro et al. (2019), Galametz et al. (2013), and Stefanon et al. (2017) for the COSMOS, GOODS-S, GOODS-N, UDS, and EGS fields, respectively. The final catalogs were compiled by combining multiwavelength observations with different spatial resolutions using the template-fitting method TFIT (Laidler et al. 2007; Lee et al. 2012), which provides uniform photometry across different filters. These catalogs also contain the photometric redshift values of the galaxies which were estimated using the method described by Dahlen et al. (2013). This method combines the posterior probability distribution of photometric redshifts from several different codes and template sets used for spectral energy distribution (SED) fitting and chooses the median of the peak redshifts of the different probability distribution functions (PDFs) as the best available photometric redshift.

To estimate the stellar masses of the galaxies, 10 different groups within the CANDELS team fit the observed multi-wavelength photometric observations with a set of SED templates with different stellar populations for a given redshift (Mobasher et al. 2015; Santini et al. 2015). These masses were then combined by computing the average of the posterior PDFs and choosing the median of the estimates as the stellar mass for a given object. Each group used their preferred fitting code, assumptions, priors, and parameter grid to determine the stellar mass using the same photometry.

For galaxies in the full ∼2 $\mathrm{deg^2}$ COSMOS field, we used the photometric catalog compiled by Laigle et al. (2016). The catalog contains photometry in 30 bands for more than half a million galaxies spanning a large redshift range up to $z \sim 6$ and their precise photometric redshifts and stellar masses. The source detection for COSMOS was also carried out using SOURCE EXTRACTOR (Bertin & Arnouts 1996). The final detection image was generated by combining NIR images from UltraVISTA with the optical broadband observations from Subaru. To estimate photometric redshifts, Laigle et al. used the NUV-band observations from GALEX, u^*-band data from the Canada–France–Hawaii Telescope (CFHT/MegaCam), as well as 6 broad bands (*B, V, g, r, i,* z^++), 12 medium bands (*IA427, IA464, IA484, IA505, IA527, IA574, IA624, IA679, IA709,*

IA738, IA767, and IA827), and two narrow bands (NB711, NB816) obtained using the Subaru SuprimeCam. SED fits were performed using the code LEPHARE[26] (Arnouts et al. 2002; Ilbert et al. 2006), which uses a wide range of templates of star-forming and quiescent galaxies from Bruzual & Charlot (2003). Extinction was added as a free parameter using the following extinction laws: Calzetti et al. (2000), Prevot et al. (1984), and Fitzpatrick & Massa (1986). The contribution of emission lines was also considered using an empirical relation between the UV radiation and the emission line flux values (Ilbert et al. 2009).

Laigle et al. (2016) use LEPHARE to estimate the stellar masses of the observed galaxies using a Chabrier (2003) IMF, two metallicities (solar and half-solar), emission lines (Ilbert et al. 2009), two attenuation curves (Calzetti et al. 2000; Arnouts et al. 2013), an exponentially declining and delayed star formation history, and a library of synthetic spectra generated based on the stellar population synthesis model of Bruzual & Charlot (2003). For the area where the COSMOS and CANDELS-COSMOS survey fields overlap, we use the CANDELS catalogs rather than COSMOS because the WFC3-selected catalog has higher angular resolution and allows us to select pairs at closer separations.

As the above-mentioned stellar masses were mostly estimated using photometric redshifts, we recompute the stellar masses of our galaxy pairs and control galaxies using the spectroscopic redshifts with the SED fitting tool Multiwavelength Analysis of Galaxy Physical Properties (MAGPHYS; da Cunha et al. 2008) using the photometry described above and the Bruzual & Charlot (2003) stellar population libraries. We choose this code as it efficiently measures stellar masses and star formation rates for galaxies in a self-consistent manner. We compare our new masses with the original ones and find that they are consistent for cases where the redshift did not change. In this paper, we use the stellar masses we recomputed with the spectroscopic redshifts unless stated otherwise. In particular, we use these stellar masses to define the final spectroscopic galaxy pair and control samples described in detail in Section 3. The star formation rates will be discussed in a subsequent paper.

2.2. X-Ray Observations

In order to identify AGNs based on X-ray emission, we used deep Chandra X-ray observations in UDS (Kocevski et al. 2018), GOODS-S (Xue et al. 2011), GOODS-N (Alexander et al. 2003), EGS (Laird et al. 2009; Nandra et al. 2015), and COSMOS (Chandra COSMOS-Legacy Survey; Elvis et al. 2009; Civano et al. 2016; Marchesi et al. 2016) with the full band (0.5–10 keV) limiting fluxes of 4.4×10^{-16}, 3.2×10^{-17}, 2.5×10^{-17}, 1.5×10^{-16}, and 9×10^{-16} erg s^{-1} cm^{-2}, respectively.

2.3. Spitzer Space Telescope Infrared Observations

To identify infrared-selected AGNs (IR AGNs), we used observations obtained with the four Infrared Array Camera (IRAC) channels (3.6, 4.5, 5.8, 8.0 μm) on the Spitzer Space Telescope in all the fields: COSMOS (Sanders et al. 2007; Ashby et al. 2013; Laigle et al. 2016), UDS (Ashby et al. 2013, 2015), GOODS (N-S) (Dickinson et al. 2003; Giavalisco et al. 2004; Ashby et al. 2013), and EGS (Barmby et al. 2008; Ashby et al. 2015).

2.4. Spectroscopic Observations

In this study, we used all known existing spectroscopic redshifts in the CANDELS and COSMOS fields, as compiled by each of the teams and assigned quality flags on a consistent system. We combined these redshifts with our own measured redshifts from our observations obtained using the DEep Imaging Multi-object Spectrograph (DEIMOS) on the Keck II telescope, described below.

For the GOODS-S field, we use spectroscopic redshift measurements obtained using observations from the Very Large Telescope (VLT)/ Visible Multi-object Spectrograph (VIMOS; Le Fèvre et al. 2004; Ravikumar et al. 2007; Balestra et al. 2010; Le Fèvre et al. 2013; McLure et al. 2018), VLT/FORS1 (FORS: the visual and near-UV FOcal Reducer and low-dispersion Spectrograph) and VLT/FORS2 (Daddi et al. 2004; Szokoly et al. 2004; van der Wel et al. 2004; Mignoli et al. 2005; Vanzella et al. 2008, 2009; Popesso et al. 2009; Balestra et al. 2010; Kurk et al. 2013; Pentericci et al. 2018), VLT/the Multi Unit Spectroscopic Explorer (MUSE) (Inami et al. 2017; Urrutia et al. 2019), HST/WFC3-IR grism spectroscopy (Ferreras et al. 2009; Morris et al. 2015; Momcheva et al. 2016), Gemini/ Gemini Multi-object Spectrographs (GMOS) (Roche et al. 2006), Keck I/Multi-object Spectrometer For Infra-Red Exploration (MOSFIRE) (Kriek et al. 2015), Keck II/DEIMOS (Silverman et al. 2010; Cooper et al. 2012c), and the Anglo-Australian Telescope (AAT)/LDSS++ spectrograph (Croom et al. 2001).

For the GOODS-N field, we use spectroscopic redshift values estimated using observations from HST/WFC3-IR grism spectroscopy (Ferreras et al. 2009; Momcheva et al. 2016), Keck I/MOSFIRE, the Low Resolution Imaging Spectrometer (LRIS) (Cowie et al. 2004; Reddy et al. 2006; Barger et al. 2008; Kriek et al. 2015; Wirth et al. 2015), Keck II/DEIMOS (Cowie et al. 2004; Wirth et al. 2004; Barger et al. 2008; Cooper et al. 2011), and the Subaru Telescope/Multi-object Infrared Camera and Spectrograph (MOIRCS; Yoshikawa et al. 2010).

The spectroscopic redshift values we use for the EGS field are based on spectroscopic observations acquired using Keck I/ MOSFIRE and LRIS (Coil et al. 2004; Kriek et al. 2015; Masters et al. 2019), Keck II/DEIMOS (Cooper et al. 2012a; Newman et al. 2013; Masters et al. 2019), and HST/WFC3-IR grism spectroscopy (Momcheva et al. 2016).

For the UDS field, we use spectroscopic redshift estimates based on observations from HST/WFC3-IR grism spectroscopy (Morris et al. 2015; Momcheva et al. 2016), VLT/VIMOS and FORS2 (Bradshaw et al. 2013; Pentericci et al. 2018), Keck I/MOSFIRE and LRIS (Kriek et al. 2015; Masters et al. 2019), Keck II/DEIMOS (Masters et al. 2019), and VLT/ VIMOS (McLure et al. 2018; Scodeggio et al. 2018).

For the COSMOS field, we use spectroscopic redshifts estimated from observations obtained using VLT/VIMOS (Lilly et al. 2007; Le Fèvre et al. 2015; Tasca et al. 2015; van der Wel et al. 2016; Straatman et al. 2018), VLT/FORS2 (Comparat et al. 2015; Pentericci et al. 2018), Keck I/ MOSFIRE and LRIS (Kriek et al. 2015; Masters et al. 2019), Keck II/DEIMOS (Capak et al. 2004; Kartaltepe et al. 2010; Hasinger et al. 2018; Masters et al. 2019), MMT/Hectospec spectrograph (Damjanov et al. 2018), Subaru/MOIRCS

[26] http://cfht.hawaii.edu/~arnouts/LEPHARE/lephare.html

(Onodera et al. 2012), Subaru/FMOS (Fiber multi-object Spectrograph; Kartaltepe et al. 2015b; Silverman et al. 2015), HST/WFC3-IR grism spectroscopy (Krogager et al. 2014; Momcheva et al. 2016), and Magellan (Baade) telescope/Inamori Magellan Areal Camera and Spectrograph (IMACS; Trump et al. 2009; Coil et al. 2011).

We also use spectroscopic observations obtained using Gemini/GMOS (I. Cox et al. 2020, in preparation) and Keck I/MOSFIRE (B. Vanderhoof et al. 2020, in preparation) for the UDS, COSMOS, and GOODS-S fields.

2.5. Keck II/DEIMOS Observations

Apart from the above-mentioned spectroscopic observations, we also include spectra of galaxies observed with DEIMOS (PI: J. Kartaltepe). DEIMOS is an optical (4000–10500 Å) multi-object imaging spectrograph mounted on the Keck II Telescope (Faber et al. 2003). In a single exposure, DEIMOS can simultaneously take spectroscopic observations of more than 100 galaxies, covering a wide spectral range of up to 5000 Å with a high spectral resolution ($R \sim 2000$ with the 600 l/mm grating). The user can specify the length, width, position, and position angle (PA) of individual slits. These characteristics make DEIMOS one of the best instruments for obtaining spectroscopic observations, and hence estimating spectroscopic redshifts, of a large number of galaxies over a wide area.

For the DEIMOS observations, we select galaxy pair candidates using stellar masses and photometric redshifts from the CANDELS team-derived catalogs using the pair selection criteria described in Section 3.1. From these galaxy pair candidates, we select those without spectroscopic redshift values available at the time to generate a target candidate list. In this list, we also include other (e.g., Herschel Space Observatory detected) galaxies without spectroscopic redshifts as fillers. We assign a higher priority to the galaxy pair candidates (primary targets) and lower to the filler galaxies (secondary targets).

To design DEIMOS slitmasks, we use the DSIMULATOR[27] slitmask software, which creates the final target list from the target candidate list. We choose positions and PAs of the masks and corresponding slits to cover both members of the galaxy pairs at the smallest separations if possible or to follow the major axis of the galaxy. We created a total of 12 masks for the observations in the CANDELS-COSMOS field and 9 masks for the CANDELS-UDS field with ∼100 targets per mask.

We observed the CANDELS-COSMOS and CANDELS-UDS fields over two observing runs—2014 December 16 and 17, and 2017 January 30. There were clouds throughout the 2014 run, which affected the data quality, so only the brightest galaxies were detected. However, the weather was clear with seeing ∼0.″5 throughout the observation night in 2017. For wavelength calibration, we carried out observations of the Ne, Ar, Kr, and Xe arc lamps. During the observation run in 2014, we observed eight slitmasks for each of the two fields and during the observation run in 2017, we observed four slitmasks for the CANDELS-COSMOS field and one slitmask for the CANDELS-UDS field. We used the 600ZD grating on the DEIMOS instrument for these observations. Each mask was observed for ∼100 minutes.

[27] https://keck.hawaii.edu/inst/deimos/dsim.html

We reduced the data using the publicly available spec2d IDL pipeline created for the DEIMOS instrument (Cooper et al. 2012b; Newman et al. 2013). The spec2d pipeline extracts sources and their corresponding sky-subtracted and calibrated one-dimensional (1D) and two-dimensional (2D) spectra. In some cases, we obtained more than one spectrum (targeted source and serendipitous source) for a given slit. For some of them, the serendipitous source was the companion galaxy of the corresponding pair candidate. For other cases, the serendipitous source(s) was (were) just a background/foreground source(s).

For the measurement of spectroscopic redshifts, we used the SpecPro software package (Masters & Capak 2011) with built-in spectroscopic templates for galaxy emission and absorption features. We visually overlaid spectroscopic templates on the common emission and absorption features of the 1D and 2D observed spectra and used photometric redshifts as initial guess values. We estimated the spectroscopic redshift by shifting the emission templates along the wavelength axis until their emission and absorption features best matched with the observed features. We defined four flags corresponding to the quality of the spectroscopic redshift value, consistent with the quality flags used by the CANDELS and COSMOS team spectroscopic compilations. Quality flag 1, 2, 3, and 4 correspond, respectively, to one spectral line with low signal-to-noise ratio (S/N), one spectral line with high S/N, multiple spectral lines with low S/N, and several spectral lines with high S/N. This scheme follows a simplified version of the flags defined by the zCOSMOS survey (Lilly et al. 2009). In the case where only one emission line was detected, we assume that it corresponded to the brightest line nearest the photometric redshift.

For the CANDELS-UDS field, we estimated spectroscopic redshifts for a total of 243 galaxies, out of which 105 have a high quality flag of 3 or 4, and 138 have a low quality flag of 1 or 2. For the CANDELS-COSMOS field, we estimated spectroscopic redshifts for a total of 261 galaxies with 118 redshift values with a high quality flag (3,4) and 143 redshift values with a low quality flag (1,2). We present the spectroscopic redshift distribution (gray line) of galaxies observed with DEIMOS in Figure 1 subdivided into low quality flag 1 (dashed red line), quality flag 2 (dotted–dashed light blue line) and high quality flag 3 and 4 (dotted–dotted–dotted–dashed navy line) quality flags. The distribution shows that most of the low redshift ($z < 1$) and high redshift ($z > 1$) estimates are dominated by high quality flags and low quality flags, respectively. This is mainly due to multiple bright lines observed for most of the low-redshift galaxies and only one bright line observed for most high-redshift galaxies.

To summarize, we use the source positions, photometric redshifts, and stellar masses from the CANDELS and COSMOS photometric catalogs to identify galaxy pair candidates for targeting with our DEIMOS observations. We use the new spectroscopic redshifts along with the existing spectroscopic redshifts gathered from the literature to recompute the stellar masses as described above and use those new stellar masses throughout our analysis.

3. Sample Selection

This section describes the criteria we use to generate (i) the spectroscopic galaxy pair sample, (ii) the visually identified interacting galaxy and merger sample, and (iii) the

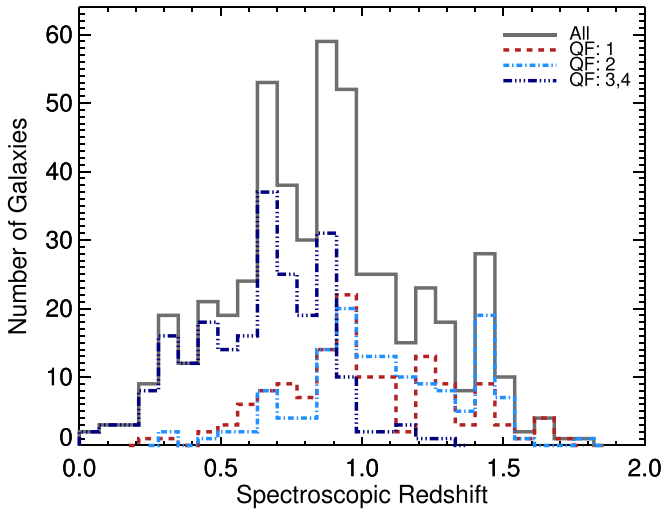

Figure 1. Distribution of spectroscopic redshift values obtained from DEIMOS observations in UDS and COSMOS (gray line) with low quality flag of 1 (dashed red line), 2 (dotted–dashed light blue line), and high quality flag 3 or 4 (dotted–dotted–dotted–dashed navy line). Most of the $z < 1$ redshifts are of high quality. Since multiple bright lines are often observed while at $z > 1$, only one strong line is typically seen and therefore assigned a quality flag of 1 or 2. Note the spike at $z \sim 0.9$, which corresponds to several overdensities in both fields between $z \sim 0.9$ and 1.

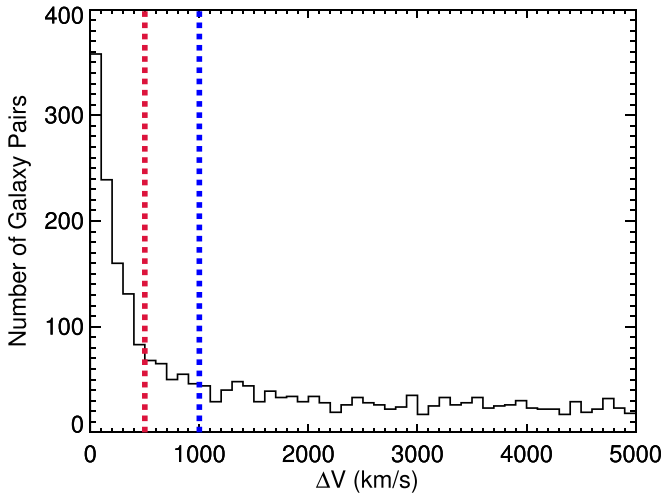

Figure 2. Relative line-of-sight velocity distribution of our sample of 2381 galaxy pairs with $\Delta V < 5000$ km s^{-1}, with vertical lines highlighting the cuts of $\Delta V < 1000$ km s^{-1} (blue) and $\Delta V < 500$ km s^{-1} (red) used throughout this paper. The sharp peak at very small velocities indicates that the majority of these pairs are likely to be interacting.

corresponding mass-, redshift-, and environment-matched isolated (control) galaxy sample using the CANDELS and COSMOS survey observations. Since AGN activity strongly depends on the stellar mass, redshift, and environment of a galaxy, in order to isolate the effect of interactions and mergers, we control for these variables by generating a mass-, redshift-, and environment-matched control sample corresponding to the galaxy pair sample.

3.1. Pair Selection

We combine the photometric and spectroscopic catalogs in the COSMOS and CANDELS fields described above to obtain the coordinates, stellar masses, and the best spectroscopic redshifts for galaxies in each field. We only use spectroscopic redshifts with quality flag greater than one based on the above-mentioned scheme for both the literature compilations and our DEIMOS observations. We only consider massive galaxy pairs undergoing major galaxy interactions by restricting the stellar mass of both galaxies in a pair to be greater than $10^{10}\,M_{\odot}$ and the stellar mass ratio of primary to secondary galaxy (less massive of the two galaxies in a pair) to be less than four, consistent with the typical values used in the literature (e.g., Ellison et al. 2013a; Mantha et al. 2018). Since the mass completeness at high redshift differs among the different CANDELS and COSMOS fields, in order to be consistent, we constrain the redshift of paired galaxies to be less than three since all of the fields are complete down to $10^{10}\,M_{\odot}$ at this redshift. As the focus of this study is on high -redshift interactions, and for $z < 0.5$ each of the CANDELS fields contains a small volume, we restrict the spectroscopic redshift of the paired galaxies to be greater than 0.5. Ideally, we would measure the three-dimensional separation between galaxies to select the companion for a galaxy. However, in reality, we can only estimate the projected separation of galaxies. We calculate the projected physical separation of the two galaxies in a pair by using their angular separation and average spectroscopic redshift. To constrain the line-of-sight separation, we use the relative radial velocities obtained using the spectroscopic redshifts of the galaxies.

We use the following criteria to generate the sample of massive spectroscopic galaxy pairs undergoing major galaxy interactions:

1. *Redshift limit*: the spectroscopic redshift of both of the galaxies in a pair has to be between 0.5 and 3.0.
2. *Mass limit*: the stellar mass of both of the galaxies has to be greater than $10^{10}\,M_{\odot}$.
3. *Stellar mass ratio*: the stellar mass ratio of the primary to the secondary galaxy has to be less than four.
4. *Relative line-of-sight velocity*: companions are required to have their relative line-of-sight velocity (obtained using their spectroscopic redshifts) within 5000 km s^{-1}. This is an intentionally large relative velocity cut that enables us to test for the effect of different cuts. We explore the effect of using a $\Delta V < 500$, 1000, and 5000 km s^{-1} selection throughout our analysis.
5. *Projected separation*: we require the projected separation between companions to be less than 150 kpc.

To explore the effects of interactions as a function of the projected separation of a galaxy pair, we intentionally include potentially merging systems as well as pairs that are interacting/have interacted in the past but are not going to necessarily merge (they could still have been affected by the interaction). Hence, we want to cover a wide range of separation and relative velocity difference. While most studies consider the maximum projected separation of a galaxy pair to be ∼80–100 kpc (e.g., Patton et al. 2011; Scudder et al. 2012; Ellison et al. 2013b), there are some studies that show that galaxy interactions can have effects on galaxy pairs with a projected separation of up to 150 kpc (e.g., Patton et al. 2013). Therefore, we restrict the maximum projected separation of galaxy pairs to 150 kpc. We only select the closest secondary galaxy for a given primary galaxy.

We present a total sample of 2381 spectroscopic major galaxy pairs satisfying all the conditions mentioned above. The relative velocity distribution of galaxy pairs satisfying all the

Table 1
Number of Major Spectroscopic Galaxy Pairs in Each Field

Field	# Galaxy Pairs		
	$\Delta V < 5000$	$\Delta V < 1000$	$\Delta V < 500$
COSMOS	1802	1008	806
UDS	127	72	52
GOODS-N	82	44	37
GOODS-S	211	140	110
EGS	159	81	61
Total	2381	1345	1066

Note. ΔV denotes relative line-of-sight velocity in km s^{-1}.

criteria is shown in Figure 2. To maximize the chances of galaxies being physically associated and therefore the possibility of interaction, and to explore the effects of using different velocity cuts, we also apply more restrictive cuts to the relative velocity difference of less than 500 km s^{-1} (1066 pairs) and 1000 km s^{-1} (1345 pairs) and explore the effect of using different velocity cuts in our results. Table 1 shows the number of galaxy pairs in each field satisfying all criteria.

The projected separation distributions of these galaxy pair samples are shown in Figure 3, which is fairly uniform at separations greater than 20 kpc. There are relatively few systems in the smallest projected separation bin (< 10 kpc). The minimum separation among the pairs in our sample is 4.4 kpc. Even with HST resolution, systems at closer separations are difficult to resolve at high redshift. Given the redshift range of our sample, the physical separation that we can resolve does not vary much with redshift. At closer separations, some pairs might be blended in our photometric measurements but are still able to be detected visually. Such systems are described in the next section.

3.2. Visually Identified Interactions and Mergers

To investigate different stages of the galaxy merger process, we also selected a subsample of visually identified interacting galaxies and mergers using the classification scheme and catalog of Kartaltepe et al. (2015a). As mentioned above, the number of spectroscopic galaxy pairs with projected separation less than 10 kpc is limited in our sample as it is hard to resolve two galaxies with small separation in a pair at high redshift. However, pairs at these separations are more likely to show morphological signatures of interaction and less likely to be chance projections. Therefore, we include visually identified pairs as well as mergers that have coalesced into a single system in order to span the full range of physical separations and merger stages. A caveat to using the visually identified sample is that the observability of the morphological signs of mergers and interactions can strongly depend on different properties of the merging galaxies such as their morphological types, stellar masses and stellar-mass ratio, redshift, gas fraction, orbital parameters of the merger, as well as observational factors such as the image depth, observed wavelength, viewing angle, etc. Hence, this sample does not represent a complete sample of interactions and mergers.

Kartaltepe et al. (2015a) produced a visual classification catalog for all galaxies with $H < 24.5$ in the CANDELS fields, covering ~50,000 galaxies in total. Each galaxy was visually classified by at least three individual classifiers. In order to construct a sample of high-confidence galaxy interactions and

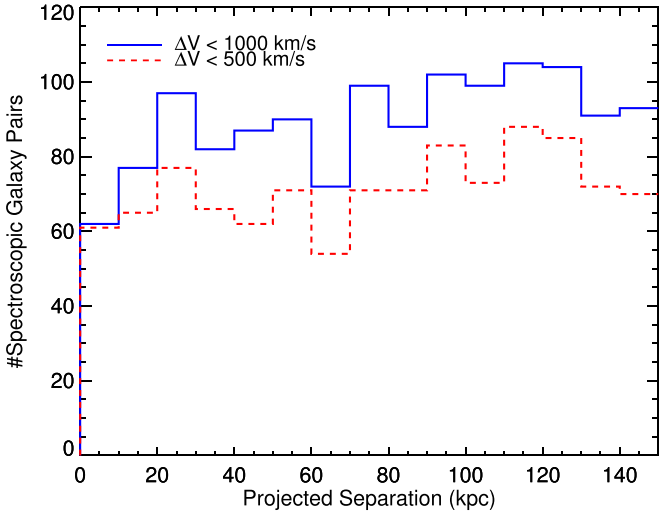

Figure 3. Projected separation distribution of galaxy pairs with $\Delta V <$ 1000 km s^{-1} (blue) and $\Delta V <$ 500 km s^{-1} (red). Note that while the overall distribution of the sample is relatively uniform, there is a dearth of pairs at the closest separations (< 10 kpc) where close pairs are hardest to resolve.

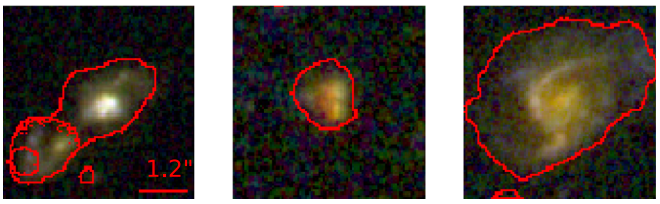

Figure 4. HST F606W, F125W, and F160W composite images of an example of a visually identified non-blended interaction (left), a blended interaction (center), and a merger (right). The red contours show the outlines of the segmentation map. All the images are the same angular size and have a 1.″2 scale bar. Note that each of these galaxies has observable tidal tails and disturbed morphology.

mergers, we selected galaxies where $\geqslant 2/3$ of all classifiers agreed that the galaxy was involved in an interaction or a merger, with additional cuts as described below. A full catalog of galaxy mergers and interactions, along with confidence classes and their properties will be published in a separate paper (C. Magagnoli et al. 2020, in preparation).

Kartaltepe et al. (2015a) define three mutually exclusive classes for potentially interacting and merging galaxies for the visual morphological classification scheme, which we will refer to here as merger, blended interaction, and non-blended interaction. We apply further constraints on galaxies in these classes to select a sample of potential high-confidence major interactions and mergers. The definitions of these classes and our further constraints are described below:

(i) *Merger*: A galaxy that shows signs of a recent merger such as tidal tails, loops, double nuclei, or highly irregular outer isophotes is classified as a merger. We apply an additional constraint on the mass of the merged system to be greater than $1.25 \times 10^{10} M_{\odot}$. If the minimum mass of the primary galaxy at a pre-merger stage is greater than $10^{10} M_{\odot}$ and the maximum mass ratio of the stellar mass of the primary to that of the secondary galaxy is 4, then the stellar mass of the merged galaxy system has to be greater than $1.25 \times 10^{10} M_{\odot}$. We also require the redshift of the mergers to be between 0.5 and 3.0. Based on these criteria, we generated a sample of 66 high-confidence

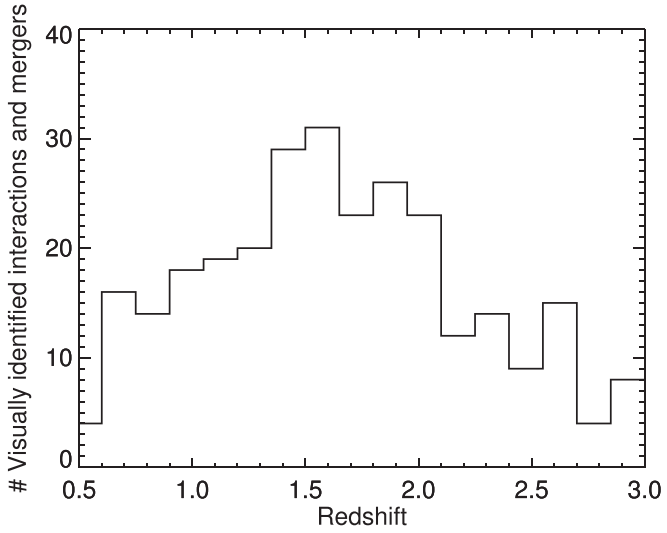

Figure 5. Photometric redshift distribution of the combined sample of visually identified high-confidence mergers, blended interactions, and non-blended interactions. Note that this sample has a broader redshift distribution than the galaxy pair sample shown in Figure 6 with a median redshift of 1.6.

major galaxy mergers. We show an example of a merger in the rightmost panel of Figure 4.

(ii) *Blended interaction*: If a galaxy pair shows clear signs of tidal interactions (e.g., tidal arms, tidal bridges, dual asymmetries, off-center isophotes, or other signs of morphological disturbance) and both galaxies are within the same *H*-band segmentation map, then the system is classified as a "blended interaction." Classifiers choose this class over the merger class if two distinct galaxies are visible. In the case of more than one companion, the class is determined by the one that seems to dominate the morphology, which is typically the larger/brighter one. Since these sources are blended, the photometry corresponds to the combined system of the two galaxies, i.e., the properties of the system, such as the stellar mass and photometric redshift, correspond to the combined system. Hence, we apply the same additional constraint on the mass of the combined system as in the merger class, i.e., the stellar mass of the combined blended system has to be greater than $1.25 \times 10^{10} M_{\odot}$. We also require the redshift value of the system to be $0.5 < z < 3.0$. We visually identify the photocenter of each of the galaxies and use the photometric redshift for the combined system to estimate the projected separation of the two galaxies. Using these constraints, we generated a sample of 100 high-confidence galaxy pair systems going through a close interaction. The median projected separation for this sample is 7.73 kpc. We show an example of a blended interaction in the middle panel of Figure 4.

(iii) *Non-blended interaction*: The only difference between this class and the "blended interaction" class is that in this class, the two interacting galaxies do not belong to the same *H*-band segmentation map so both galaxies have their own measurements of the photometric properties. Hence, we apply constraints to both galaxies. The stellar mass of the secondary galaxy has to be greater than $10^{10} M_{\odot}$, the stellar mass ratio of the primary to secondary galaxy has to be less than four, and their photometric redshift error bars have to overlap with each other. Our sample of non-blended interactions consists of 61 galaxy pairs, i.e., 122 galaxies. The leftmost image in Figure 4 shows an example of a non-blended interaction, showing two distinct galaxies in different segmentation maps with visible signs of interaction such as tidal tails. The median projected separation for this sample is 13.15 kpc.

Figure 5 shows the photometric redshift distribution of the combined sample of high-confidence mergers, blended interactions, and non-blended interactions. The photometric redshift distribution of the visually identified mergers and interactions (median $z \sim 1.6$) is much broader than the spectroscopic redshift distribution of the pair sample (median $z \sim 1$).

3.3. Control Samples

To isolate the effects of galaxy interactions on galaxy properties, the effects of other strongly variable properties affecting AGN activity like the stellar mass, redshift, and environment of the galaxy have to be controlled for. The distribution of these properties for the paired galaxies could be significantly different from the overall distribution of galaxies. Therefore, if we randomly select isolated galaxies, the distribution of their properties (such as mass, redshift, and environmental density) could be different from that of the pairs. We select a sample of isolated galaxies with similar stellar mass, redshift, and environment distributions as our paired galaxies. Since the spectroscopic completeness varies with each field and is highly correlated with properties such as stellar mass, star formation rate, and the presence of an AGN, we require our controls for the galaxy pair sample to have spectroscopic redshifts and to be selected from the same field. For the control sample for the visually identified and interactions and mergers, we do not require spectroscopic redshifts.

We create a parent sample of isolated galaxies with no major or minor companion (within a mass ratio of 10) within a Δz corresponding to a relative velocity of less than 5000 km s^{-1}, out to a projected separation of 150 kpc. We also exclude the visually identified interactions and mergers described in the previous sub-section from the control candidate samples. We then match the mass, redshift, and local galaxy environment of the controls with that of the paired galaxies. The environmental overdensity (ratio of the density around the position and redshift of the galaxy to that of the median density in that redshift bin) for galaxies in the COSMOS field was estimated using redshift-dependent "weighted" adaptive kernel density maps generated by Darvish et al. (2015). For the CANDELS fields, the density estimation was carried out using the Voronoi Tessellation method described by Lemaux et al. (2017) and Tomczak et al. (2017). Though these methods are slightly different, previous work has shown that the results are consistent with one another (Darvish et al. 2015), and we find no significant systematic differences. In both cases, we calculated the overdensity from the density measurements in a consistent way.

To generate the final control sample, for each galaxy in our galaxy pair sample, we select three control galaxies from the above-mentioned control parent sample by minimizing $(\Delta \log M_*)^2 + (\Delta z)^2 + (1/40)(\Delta \mathrm{overdensity})^2$. Considering the range and distribution of overdensity, redshift, and stellar mass, we used a weighing factor of $1/40$ for the overdensity to obtain the best match in all three dimensions so that the

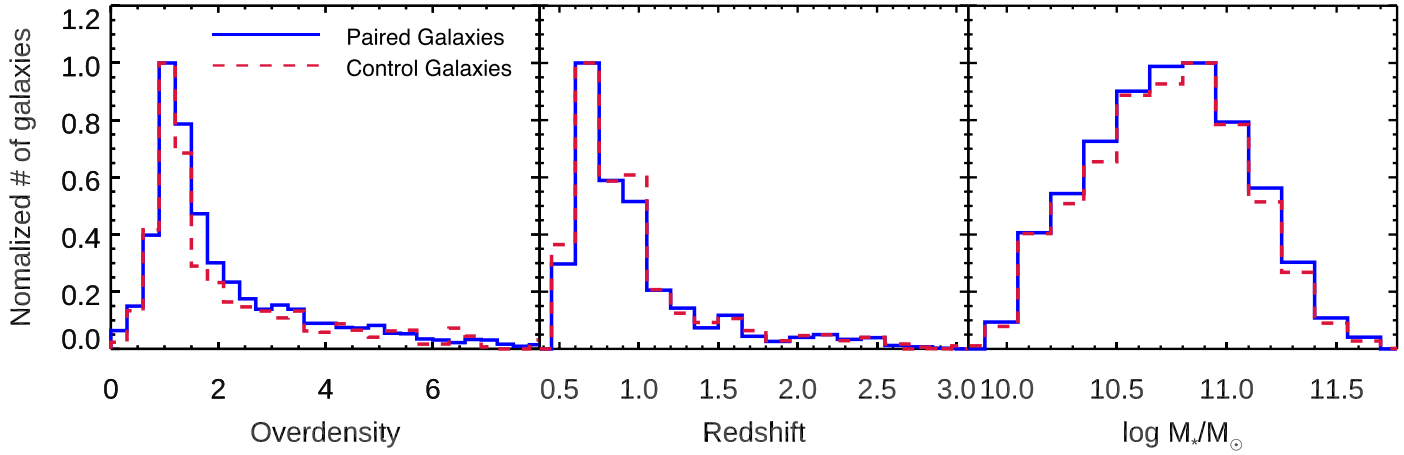

Figure 6. Environmental overdensity (left panel), spectroscopic redshift (middle panel), and stellar mass (right panel) distributions (normalized to the peak value) of 1345 spectroscopic galaxy pairs (solid blue line) (satisfying $\Delta V < 1000$ km s^{-1}, projected separation < 150 kpc, mass ratio < 4, and spectroscopic redshift between 0.5 and 3) and the corresponding mass-, redshift-, and environment-matched control galaxies (red dashed line).

overdensity-matching does not dominate. For more than 90% of paired galaxies, the controls match within a stellar mass of 0.15 dex, spectroscopic redshift within 0.15, and overdensity within 1. Our final control sample contains 8070 (6399) control galaxies for pairs with $\Delta V < 1000(500)$ km s^{-1}, out of which 8034 (6374) galaxies are unique.

The normalized environmental overdensity, redshift, and stellar mass distribution of the final galaxy pair sample and corresponding control galaxy sample is shown in Figure 6. The distribution of these quantities as a function of the projected separation is shown in Figure 7. These plots show that the galaxy pairs and controls have similar environmental overdensity, redshift, and stellar mass distributions, crucial for our analysis. The middle panel in Figure 6 shows that the number of paired galaxies increases with redshift out to $z \sim 0.8$ and then decreases, with a median value of 1.0. The right panel shows that the sample is mostly uniform for masses between about 10^{10} $M_\odot$ and 10^{11} $M_\odot$, after which it rapidly decreases for increasing mass, with very few galaxies above $10^{11.5}$ $M_\odot$. Figure 7 shows that while the paired galaxy sample spans a wide range of mass, redshift, and environmental overdensity, the median value of these properties does not vary significantly with the projected separation.

4. Analysis of AGN Activity

In this section, we discuss the identification of AGNs in the X-ray and IR and measurement of the AGN fraction for the spectroscopic paired galaxies, visually identified mergers and interactions, and control galaxies. We then estimate the level of AGN enhancement and its dependence on the projected separation of galaxy interactions.

4.1. AGN Identification

4.1.1. X-Ray AGNs

We use the Chandra X-ray observations (Section 2.2) to identify X-ray-selected AGNs. For the X-ray sources among the spectroscopic pairs and their corresponding control samples, we computed the total X-ray luminosity L_X following the method of Marchesi et al. (2016), using the spectroscopic redshift z) and X-ray flux (F_X) values in

$$L_X = F_X \times 4\pi d^2 \times k(z), \quad (1)$$

where

$$k(z) = (1+z)^{(\Gamma-2)}, \quad (2)$$

d is the luminosity distance for a given redshift, $k(z)$ is the k-correction, and $\Gamma = 1.4$ is the slope of the power law (Marchesi et al. 2016). We identify the sources with a total (full band: 0.5–10 keV) X-ray luminosity of greater than 10^{42} erg s^{-1} as X-ray AGNs (e.g., Moran et al. 1999). This luminosity cut ensures that the observed flux is almost completely dominated by the AGNs and the contamination due to star formation is negligible. Although this requirement may miss many low luminosity and/or highly dust-obscured AGNs, in comparison with other selection methods (e.g., optical, IR, radio), X-ray identification of AGNs provides a clean AGN sample.

4.1.2. IR AGNs

We use the Spitzer/IRAC observations described in Section 2.3 to identify IR AGNs using two different sets of selection criteria (Stern et al. 2005; Donley et al. 2012). While the Stern et al. (2005) criteria select a more complete sample of AGNs, this sample is also subject to a large amount of contamination from star formation, while the Donley et al. (2012) selected sample is less contaminated but also less complete. We include both samples in our analysis for comparison.

Galaxies with dominant AGN emission usually follow a characteristic red power law in the IR ($f_\nu \propto \nu^\alpha$ with $\alpha \leqslant -0.5$; Alonso-Herrero et al. 2006). Therefore, IR power-law selection can be used to select a clean AGN sample. The Donley et al. (2012) criteria provide reliable identification of luminous AGNs with minimal contamination from star formation. To satisfy the Donley et al. (2012) criteria, objects must be detected in all four IRAC bands, and their colors must lie within the following IRAC color–color region:

$$x = \log_{10}\left(\frac{f_{5.8\,\mu m}}{f_{3.6\,\mu m}}\right),\ y = \log_{10}\left(\frac{f_{8.0\,\mu m}}{f_{4.5\,\mu m}}\right), \quad (3)$$

$$x \geqslant 0.08 \ \wedge \ y \geqslant 0.15, \quad (4)$$

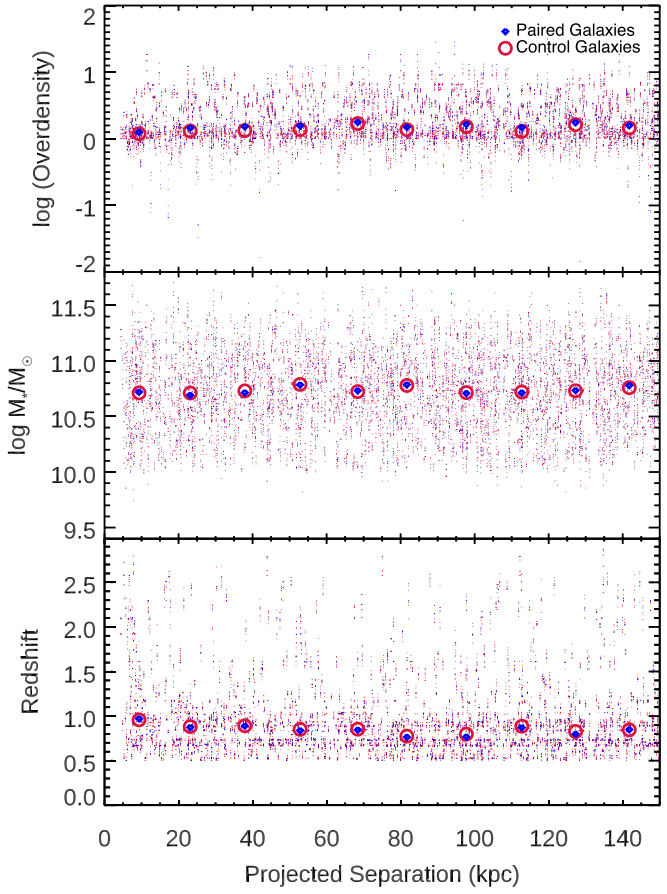

Figure 7. Small dots show the redshift (lower panel), stellar mass (middle panel), and overdensity (upper panel) values of individual paired (blue) and their corresponding control (red) galaxies as a function of the projected separation of the paired galaxies. For control galaxies, the projected separation value of the corresponding paired galaxy is used. The median properties of all the paired and control galaxies within projected separation bins of 10 kpc width are shown by blue diamonds and red open circles, respectively. While the paired galaxy sample spans a wide range of mass, redshift, and environmental overdensity, the median values of these properties do not vary significantly with the projected separation.

$$y \geqslant (1.21 \times x) - 0.27 \ \wedge \ y \leqslant (1.21 \times x) + 0.27, \quad (5)$$

$$f_{4.5\,\mu\mathrm{m}} > f_{3.6\,\mu\mathrm{m}} \wedge f_{5.8\,\mu\mathrm{m}} > f_{4.5\,\mu\mathrm{m}} \wedge f_{8.0\,\mu\mathrm{m}} > f_{5.8\,\mu\mathrm{m}}, \quad (6)$$

where f_λ is the flux of the galaxy at wavelength λ, and "$\wedge$" is the logical "AND" operator. Using these criteria, we identify 31 Donley IR AGNs in the paired galaxy sample, and 99 AGNs in the control galaxy sample. The combined sample of visually identified mergers and interactions contains 5 Donley IR AGNs, and their control sample contains 19 AGNs.

The Stern et al. (2005) IRAC color–color selection criteria used to identify IR AGNs is defined as

$$([5.8] - [8.0]) > 0.6, \quad (7)$$

$$([3.6] - [4.5]) > 0.2 \times ([5.8] - [8.0]) + 0.18, \quad (8)$$

$$([3.6] - [4.5]) > 2.5 \times ([5.8] - [8.0]) - 3.5, \quad (9)$$

where $[\lambda]$ is the Vega magnitude of the galaxy at wavelength λ in μm. Using these criteria, we identify 106 Stern IR AGNs in paired galaxies and 296 in control galaxies. The combined sample of visually identified mergers and interactions has 47, and their combined control sample has 129 Stern IR AGNs.

There are six paired and 35 corresponding control galaxies that have both X-ray and IR AGNs (using the Donley et al. 2012 criteria). There are too few objects in this overlapping sample to allow us to analyze how the fraction of these relates to other properties such as redshift or pair separation. There are four galaxies in the visually identified interaction and merger sample and eight corresponding control galaxies that have both X-ray and IR AGNs. In total, there are 194 paired galaxies and 584 control galaxies that have either X-ray or IR AGNs. Likewise, there are 28 galaxies in the visually identified interaction and merger sample and 78 galaxies in the corresponding control samples have either X-ray or IR AGNs.

4.2. AGN Enhancement in Spectroscopic Galaxy Pairs

To estimate the level of AGN enhancement in our galaxy pair sample relative to the control galaxies, we divide the sample of galaxy pairs into projected separation bins (depending on the number of AGNs in a given bin) with a width of 25 kpc (6 bins) or 50 kpc (3 bins). We define the X-ray (or IR) AGN fraction as the ratio of the total number of galaxies having an X-ray (or IR) AGN to that of the total number of galaxies, i.e,

$$\text{AGN Fraction} = \frac{\#\ \text{AGN}}{\#\ \text{Total}}, \quad (10)$$

where AGN Fraction is for paired (control) galaxies within a given projected separation bin, # AGN is the number of paired (control) galaxies with an AGN in the given projected separation bin, and # Total is the total number of paired (control) galaxies in the given projected separation bin. For each separation bin, we calculate the AGN fraction in the paired galaxy sample and the corresponding control galaxy sample.

For the $\Delta V < 1000\,\mathrm{km\,s^{-1}}$ kinematic pair sample, the left panel of Figure 8 shows the X-ray AGN fraction for six different projected separation bins of width 25 kpc each. While there is a slight increase in the AGN fraction of the paired galaxies with decreasing separation (with a value of $8.4^{+1.6}_{-1.2}\%$ at < 25 kpc), the AGN fraction of the control sample also slightly increases. The right panel of Figure 8 shows the IR AGN fraction using the Stern et al. (2005) selection criteria for the same six projected separation bins. Just as for the X-ray AGN fraction, the IR AGN fraction of paired galaxies increases with decreasing projected separation, with a value of $6.3^{+1.47}_{-1.02}\%$ at < 25 kpc. However, the AGN fraction of the controls also increases in a similar manner. For all bins, the AGN fraction of pairs and controls are similar to each other.

We then define the AGN enhancement as the ratio of the AGN fraction of paired galaxies to that of the corresponding control galaxies, i.e,

$$\text{AGN Enhancement} = \frac{\text{AGN Fraction}_{\text{Pairs}}}{\text{AGN Fraction}_{\text{Controls}}}, \quad (11)$$

where $\text{AGN Fraction}_{\text{Pairs}}$ and $\text{AGN Fraction}_{\text{Controls}}$ are the AGN fraction values of the paired and control galaxy samples, respectively, in a given projected separation bin. We assume binomial statistics to calculate 1σ errors (Cameron 2011) in the AGN fraction, and then propagate them to compute the errors in AGN enhancement. Throughout this work, we carry out a separate analysis for X-ray and IR AGN enhancements.

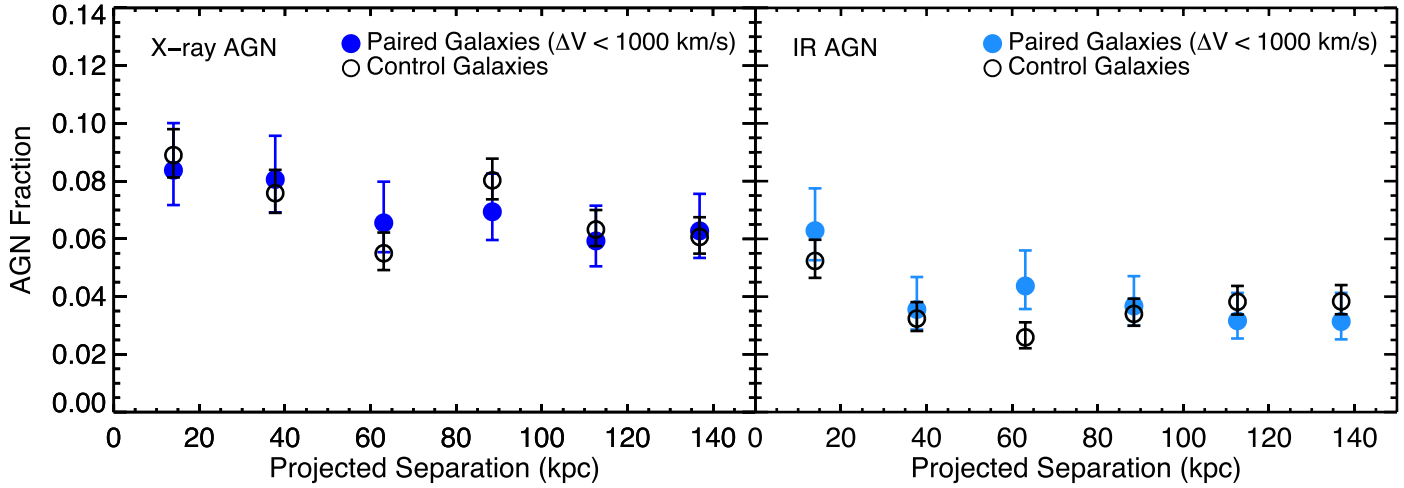

Figure 8. (left: X-ray, right: IR) AGN fraction (defined by the ratio of the number of galaxies with an AGN to that of the total number of galaxies in a given projected separation bin). The paired galaxies ($\Delta V < 1000$ km s^{-1}) are indicated by dark blue filled circles, and light blue filled circles, respectively. The black open circles in both panels show the corresponding mass-, redshift- and environment-matched control galaxies. The error bars on each point reflect the 1σ binomial confidence limits, following the method of Cameron (2011). IR AGNs are identified using Stern et al. (2005) criteria. In both panels, the AGN fraction in paired galaxies slightly increases with decreasing separation. However, the AGN fraction of the control sample also increases.

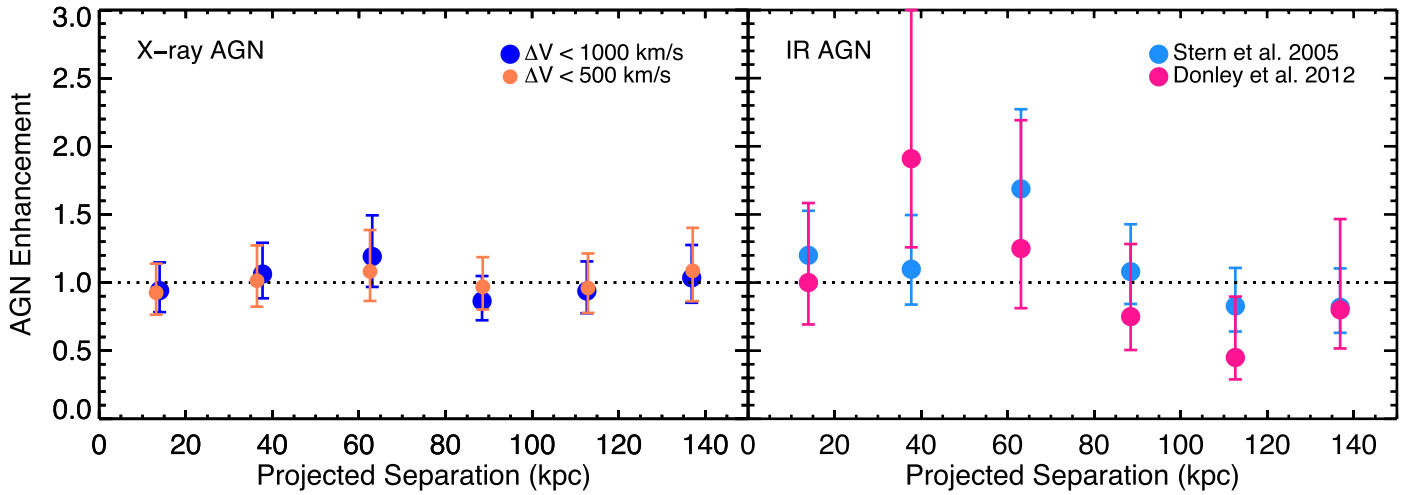

Figure 9. Level of (left: X-ray, right: IR) AGN enhancement (defined by the ratio of the AGN fraction of paired galaxies to that of the corresponding control galaxies) as a function of the projected separation of the paired galaxies. The error bars on each point reflect the 1σ binomial confidence limits, following the method of Cameron (2011). The horizontal dashed line corresponds to an AGN enhancement value of one, i.e., the AGN fraction of the paired galaxy sample is the same as the AGN fraction of the corresponding control sample and therefore signify an absence of interaction-induced AGN enhancement. Left panel: the dark blue filled circles and orange filled smaller circles correspond to the spectroscopic galaxy pairs with $\Delta V < 1000$ km s^{-1} and $\Delta V < 500$ km s^{-1}, respectively. Right panel: the IR AGN identification is based on the selection criteria of Stern et al. (2005;light blue filled circle) and Donley et al. (2012) (deep pink filled circles) applied to the IRAC observations of paired ($\Delta V < 1000$ km s^{-1}) and control galaxies. The X-ray and IR enhancement values for the paired galaxy sample with $\Delta V < 1000$ km s^{-1} are provided in Tables 2 and 3, respectively.

Table 2
X-Ray AGN Enhancement: All Fields ($L_X > 10^{42}$ erg s^{-1}, $0.5 < z < 3.0$, $\Delta V < 1000$ km s^{-1})

	$0 < d < 25$	$25 < d < 50$	$50 < d < 75$	$75 < d < 100$	$100 < d < 125$	$125 < d < 150$
Paired Galaxies	382	422	412	490	506	478
AGNs	32	34	27	34	30	30
AGN Fraction (%)	$8.4^{+1.6}_{-1.2}$	$8.1^{+1.5}_{-1.1}$	$6.6^{+1.4}_{-1.0}$	$6.9^{+1.3}_{-0.9}$	$5.9^{+1.2}_{-0.8}$	$6.3^{+1.3}_{-0.9}$
Control Galaxies	1146	1266	1236	1470	1518	1434
AGNs	102	96	68	118	96	87
AGN Fraction (%)	$8.9^{+0.9}_{-0.8}$	$7.6^{+0.8}_{-0.7}$	$5.5^{+0.7}_{-0.6}$	$8.0^{+0.8}_{-0.7}$	$6.3^{+0.7}_{-0.6}$	$6.1^{+0.7}_{-0.6}$
AGN Enhancement	$0.94^{+0.21}_{-0.16}$	$1.06^{+0.23}_{-0.18}$	$1.19^{+0.30}_{-0.22}$	$0.86^{+0.18}_{-0.14}$	$0.94^{+0.22}_{-0.16}$	$1.03^{+0.24}_{-0.18}$

Note. The projected separation(d) is measured in kpc.

Table 3
IR AGN Enhancement: All Fields (Donley et al. (2012) Criteria, $0.5 < z < 3.0$, $\Delta V < 1000$ km s^{-1})

	$0 < d < 25$	$25 < d < 50$	$50 < d < 75$	$75 < d < 100$	$100 < d < 125$	$125 < d < 150$
Paired Galaxies	382	422	412	490	506	478
AGNs	7	7	5	5	3	4
AGN Fraction (%)	$1.8^{+0.9}_{-0.5}$	$1.7^{+0.9}_{-0.4}$	$1.2^{+0.8}_{-0.3}$	$1.0^{+0.7}_{-0.3}$	$0.6^{+0.6}_{-0.2}$	$0.8^{+0.6}_{-0.3}$
Control Galaxies	1146	1266	1236	1470	1518	1434
AGNs	21	11	12	20	20	15
AGN Fraction (%)	$1.8^{+0.5}_{-0.3}$	$0.9^{+0.3}_{-0.2}$	$0.9^{+0.4}_{-0.2}$	$1.4^{+0.4}_{-0.2}$	$1.3^{+0.4}_{-0.2}$	$1.0^{+0.3}_{-0.2}$
AGN Enhancement	$1.00^{+0.58}_{-0.31}$	$1.90^{+1.25}_{-0.65}$	$1.25^{+0.94}_{-0.44}$	$0.75^{+0.53}_{-0.25}$	$0.45^{+0.45}_{-0.16}$	$0.80^{+0.66}_{-0.28}$

Note. The projected separation(d) is measured in kpc.

We calculate the X-ray AGN enhancement for spectroscopic galaxy pairs and present the results in the left panel of Figure 9 and Table 2 for both the $\Delta V < 1000$ km s^{-1} and the $\Delta V < 500$ km s^{-1} samples. The horizontal dashed line corresponds to an AGN enhancement value of one, i.e., the AGN fraction of the paired galaxy sample is the same as the AGN fraction of its control sample, therefore, indicating an absence of enhancement. We find an AGN enhancement of $0.94^{+0.21}_{-0.16}$ for the closest separation bin for pairs with $\Delta V < 1000$ km s^{-1}. We do not find a statistically significant enhancement at any separation for any of the velocity cuts used. The results of both samples are consistent with each other, which could be due to the fact that galaxies with $\Delta V < 500$ km s^{-1} dominate the $\Delta V < 1000$ km s^{-1} sample. Table 2 presents the values of the number of paired and their corresponding control galaxies, the number of X-ray AGNs and AGN fraction in these samples, and the corresponding X-ray AGN enhancement in the paired galaxies used for Figure 9. These values include the full sample of X-ray AGNs at all luminosities across the complete redshift range of $0.5 < z < 3$ with $\Delta V < 1000$ km s^{-1}.

The right panel of Figure 9 shows the level of IR AGN enhancement in the $\Delta V < 1000$ km s^{-1} kinematic pair sample at $0.5 < z < 3.0$ using both the Stern et al. (2005) and Donley et al. (2012) criteria. Since the $\Delta V < 500$ km s^{-1} sample is significantly smaller with a limited number of Donley IR AGNs, we do not include it here. At the smallest separation, we calculate the Donley IR AGN enhancement to be $1.00^{+0.58}_{-0.31}$ and the Stern IR AGN enhancement to be $1.06^{+0.38}_{-0.26}$, consistent within error bars. Table 3 includes the values used for the Donley et al. (2012) criteria identified AGN enhancement. We do not find a statistically significant enhancement for IR AGNs in any separation bin. In the figure, the error bars for the Stern IR AGNs are smaller than the error bars for the Donley IR AGNs since the Stern et al. (2005) criteria identify a larger number of AGNs than the Donley et al. (2012) criteria. We also tested the effect of applying different S/N cuts to the IRAC fluxes and do not find a significant difference when using S/N > 3 or S/N > 5 cut.

We find a similar result (no significant enhancement) when considering the combined X-ray and IR AGN sample. There are 194 paired galaxies in this category, i.e., pairs in which at least one galaxy contains either X-ray or IR AGNs. Furthermore, six paired galaxies have both an X-ray and IR-selected AGN, but there are too few AGNs to be further divided into bins for analysis.

The depth (and therefore the sensitivity) of the Chandra X-ray observations varies over the CANDELS and COSMOS fields. Figure 10 shows the total (0.5–10 keV) X-ray luminosity (L_X) distribution as a function of redshift for all X-ray AGNs in all fields, highlighting that the GOODS fields have the deepest and the COSMOS field has the shallowest X-ray observations. Since our galaxy pair and control samples consist of galaxies from all of the above-mentioned fields and we want to compare similar types of AGNs across different fields at different redshifts, it is necessary to be consistent and use the same constraints to select AGNs with similar luminosities from all the fields.

Considering the variation in X-ray completeness for the different fields, we apply three different luminosity–redshift ($L_X - z$) cuts as defined in Table 4 and Figure 10 to identify X-ray-selected AGNs in paired and control galaxies: (i) low L_X AGNs: $42 < \log(L_X(\mathrm{erg\ s^{-1}})) < 43.2$ and $0.5 < z < 2.0$ for the GOODS (North and South) fields, (ii) moderate L_X AGNs: $43.2 < \log(L_X(\mathrm{erg\ s^{-1}})) < 43.7$ and $0.5 < z < 2.0$ for all fields, (iii) high L_X AGNs: $\log(L_X(\mathrm{erg\ s^{-1}})) > 43.7$ and $0.5 > z < 3.0$ for all fields, corresponding to high-luminosity AGNs and dominated by quasars ($\log(L_X) > 44$).

The X-ray AGN enhancement for these X-ray complete $L_X - z$ cut bins in the $\Delta V < 1000$ km s^{-1} and $\Delta V < 500$ km s^{-1} pairs samples are shown in Figure 11. The lower, middle, and upper panels correspond to the Low L_X, Moderate L_X, and High L_X bins, respectively. The X-ray AGN enhancement results for the $\Delta V < 1000$ km s^{-1} pair sample are presented in Table 5. We do not see any significant enhancement in any of the three luminosity bins at any separation. The results do not change significantly if we use a stricter cut on the relative velocity difference ($\Delta V < 500$ km s^{-1}) as shown in the figure. The $\Delta V < 1000$ km s^{-1} value is sightly elevated for the largest separation bin at low Lx, however, the $\Delta V < 500$ km s^{-1} value shows the opposite. The deviation of these enhancement values from a value of one (no enhancement) is not statistically significant due to the small number of AGNs in these bins.

To investigate the level of interaction-induced X-ray AGN enhancement at different redshift epochs, we calculate the X-ray AGN enhancement in two redshift bins at the median redshift ($z\sim1$) of our spectroscopic pair sample: low-z ($z < 1$) and high-z ($z > 1$) bins. We show our results in Figure 12, and find no statistically significant difference between the low-z and high-z AGN enhancement levels.

4.3. AGN Enhancement in Visually Identified Interaction and Merger Sample

We also analyze the level of AGN enhancement in our visually identified merger and interaction samples. We split the samples into two different redshift bins separated at the median

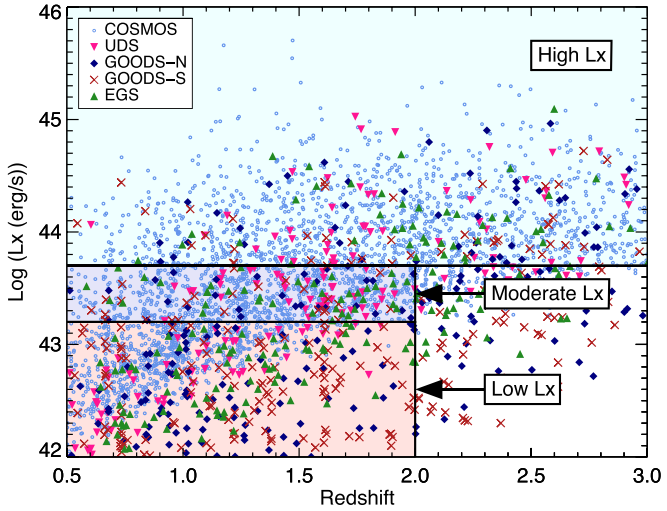

Figure 10. The distribution of the total, i.e., full band (0.5 keV – 10 keV) X-ray luminosity (L_X) with respect to redshift for all X-ray AGNs ($L_X > 10^{42}$ erg s^{-1}) in the COSMOS and CANDELS fields. In the plot, the pink downward triangles, navy diamonds, maroon crosses, green upward triangles, and small light blue circles correspond to all X-ray AGNs in UDS, GOODS-N, GOODS-S, EGS, and COSMOS, respectively. Highlighted are the three $L_X - z$ bins used in our analysis. The light red shaded region (Low L_X bin) show X-ray sources with $42.0 < \log(L_X) < 43.2$ at $0.5 < z < 2.0$ in the GOODS fields. The lavender (Moderate L_X: $43.2 < \log(L_X) < 43.7$) and light blue shaded (High L_X: $43.7 < \log(L_X)$) regions correspond to sources in all the fields with $0 < z < 2$ and $0 < z < 3$, respectively.

Table 4
X-Ray Luminosity–Redshift ($L_X - z$) Bins Used for Analysis

Panel	$\log(L_X(\text{erg s}^{-1}))$	Redshift (z)	Field(s)
Low L_X	$42.0 < \log(L_X) < 43.2$	$0.5 < z < 2.0$	GOODS
Moderate L_X	$43.2 < \log(L_X) < 43.7$	$0.5 < z < 2.0$	All
High L_X	$43.7 < \log(L_X)$	$0.5 < z < 3.0$	All

Note. L_X denotes the full band (0.5–10 keV) X-ray luminosity of a galaxy in erg s^{-1}.

redshift of the combined samples ($z \sim 1.6$). We show our results for the X-ray AGN enhancement of the complete ($0.5 < z < 3.0$) merger and interaction samples as well as for the low-z and high-z samples in Figure 13 and Table 6. Though the number of AGNs in the different redshift bins is small, and therefore the errors on the AGN enhancement value are large, we see a slight trend of increasing AGN enhancement with decreasing separation at all redshifts. Additionally, the merger and blended interaction samples have smaller enhancement values at high z compared to low z; however, the error bars are too large to make a statistically robust claim of redshift evolution.

We also calculate the IR AGN enhancement for the visually identified merger and interaction samples and show the results in Figure 14 in the same redshift bins mentioned above. We present the corresponding Stern et al. (2005) and Donley et al. (2012) criteria identified IR AGN enhancement in Table 7 and Table 8, respectively. As the number of AGNs identified using these criteria is low, the error bars on the AGN enhancement value are large, and we do not see any enhancement. Since there is a larger number of AGNs identified using the Stern et al. (2005) criteria, the error bars are smaller. However, we do

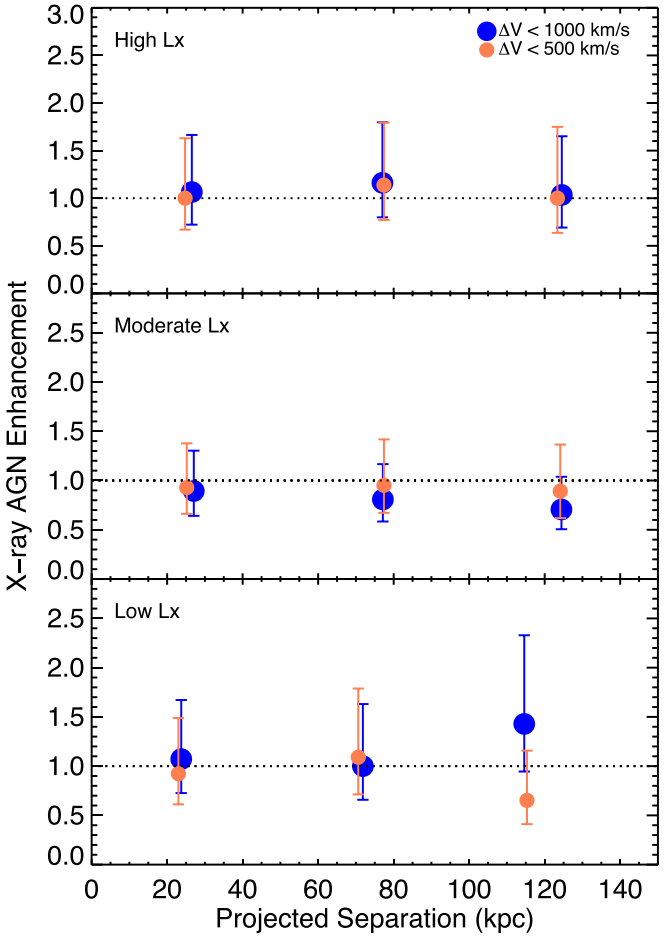

Figure 11. The X-ray AGN enhancement as a function of the projected separation of the paired galaxies with $\Delta V < 1000$ km s^{-1} (large filled blue circles) and $\Delta V < 500$ km s^{-1} (small filled orange circles), split into three different $L_X - z$ bins. The lower panel (Low L_X bin) corresponds to the galaxies in the GOODS-North and GOODS-South fields with $0.5 < z < 2.0$ and $42.0 < \log(L_X) < 43.2$. The middle panel (Moderate L_X bin) corresponds to the galaxies in all fields (CANDELS and the full COSMOS field) with $0.5 < z < 2.0$ and $43.2 < \log(L_X) < 43.7$. The upper panel (High L_X bin) corresponds to galaxies in all the fields with $0.5 < z < 3.0$ and $43.2 < \log(L_X) < 43.7$. The values of the luminosity cut at a given redshift are chosen based on X-ray completeness. The symbols for the pair sample match those in the left panel of Figure 9. The $L_X - z$ bins are defined in Table 4 and illustrated in Figure 10.

not see any enhancement for the full sample at any separation. We further divide the Stern IR AGN enhancement values for the two redshift bins and find no significant level of enhancement overall at either redshift. In the low-redshift bin, we see a slight enhancement for the non-blended interaction sample, which could indicate that enhancement is seen at an earlier stage of the merger process.

5. Discussion

To investigate the role of galaxy interactions and mergers on enhancing AGN activity at high redshift, we have compiled the largest known sample of major spectroscopically confirmed galaxy pairs at $0.5 < z < 3.0$, identified X-ray and IR AGNs among them and calculated the AGN fraction and level of AGN enhancement relative to a control sample of mass-, redshift-, and environment-matched isolated galaxies. We find that over this redshift range, major spectroscopic galaxy pairs, as well as visually identified interactions and mergers, do not

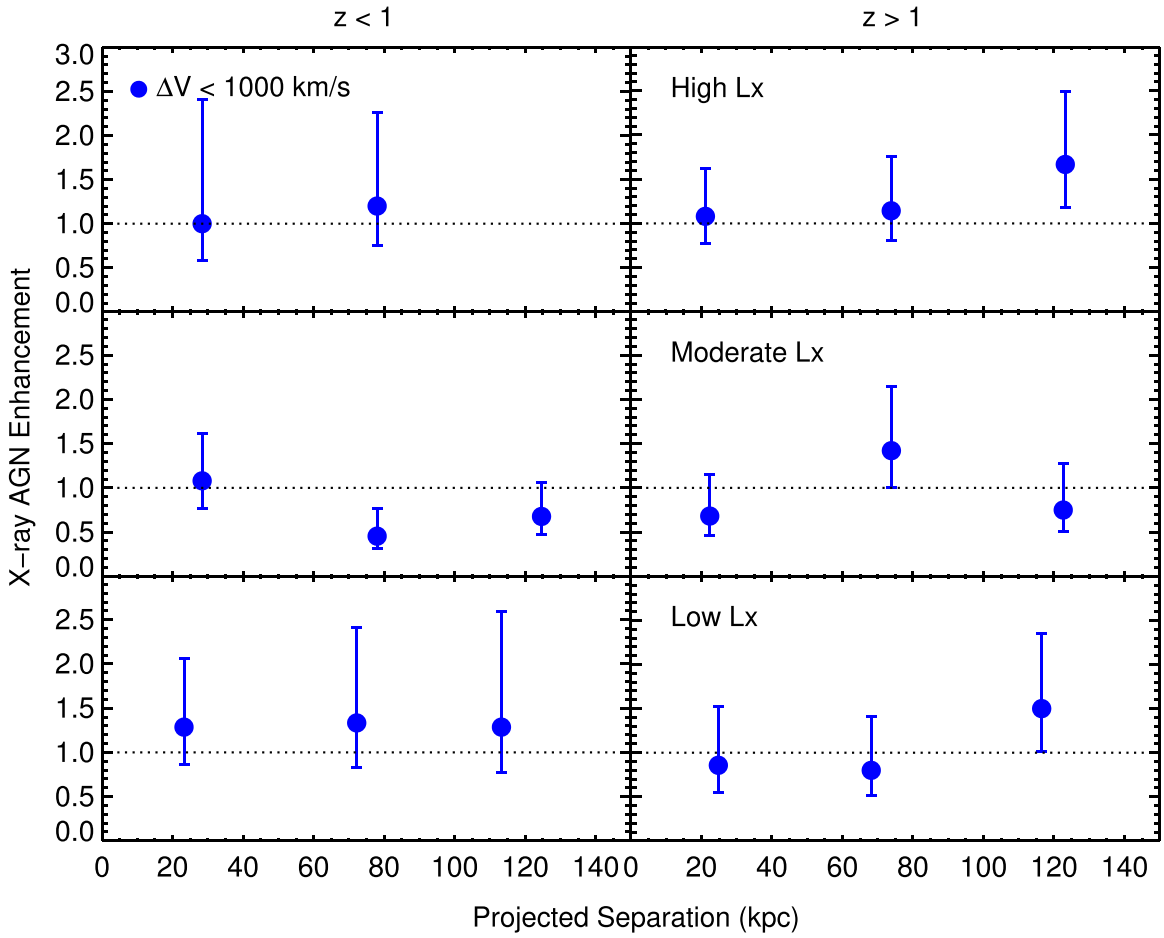

Figure 12. X-ray AGN enhancement as a function of projected separation for our sample of spectroscopically confirmed galaxy pairs with $\Delta V < 1000$ km s^{-1}, divided into redshift and X-ray luminosity bins, as defined in Table 4 Figure 10. The left and right panels correspond to $0.5 < z < 1.0$ and $1.0 < z < 3.0$, respectively. We see no significant AGN enhancement in any of our separation, redshift, or luminosity bins. At the highest separation in the high L_X bin at $z < 1$ no point is plotted since there are no AGNs in the paired galaxies satisfying these criteria.

Table 5
X-Ray AGN Enhancement in $\Delta V < 1000$ km s^{-1} Sample in Different $L_X - z$ Bins: Figure 11

	Low L_X			Moderate L_X			High L_X		
	d[0,50]	d[50,100]	d[100,150]	d[0,50]	d[50,100]	d[100,150]	d[0,50]	d[50,100]	d[100,150]
Paired Galaxies	116	98	116	742	876	926	804	902	984
AGNs	10	8	10	14	14	12	11	12	10
AGN Fraction (%)	$8.6^{+3.3}_{-1.9}$	$8.2^{+3.6}_{-1.9}$	$8.6^{+3.3}_{-1.9}$	$1.9^{+0.6}_{-0.4}$	$1.6^{+0.5}_{-0.3}$	$1.3^{+0.5}_{-0.3}$	$1.4^{+0.5}_{-0.3}$	$1.3^{+0.5}_{-0.3}$	$1.0^{+0.4}_{-0.2}$
Control Galaxies	348	294	348	2226	2628	2778	2412	2706	2952
AGNs	28	24	21	47	52	51	31	31	29
AGN Fraction (%)	$8.0^{+1.7}_{-1.2}$	$8.1^{+1.9}_{-1.3}$	$6.0^{+1.5}_{-1.0}$	$2.1^{+0.3}_{-0.3}$	$2.0^{+0.3}_{-0.2}$	$1.8^{+0.3}_{-0.2}$	$1.3^{+0.3}_{-0.2}$	$1.1^{+0.2}_{-0.2}$	$1.0^{+0.2}_{-0.2}$
AGN Enhancement	$1.07^{+0.60}_{-0.35}$	$1.00^{+0.63}_{-0.34}$	$1.43^{+0.90}_{-0.48}$	$0.89^{+0.41}_{-0.25}$	$0.81^{+0.36}_{-0.22}$	$0.71^{+0.33}_{-0.20}$	$1.06^{+0.60}_{-0.34}$	$1.16^{+0.63}_{-0.36}$	$1.03^{+0.62}_{-0.34}$

Note. $d[x, y]$: $x <$ Projected separation $(d/\mathrm{kpc}) < y$.

show any statistically significant IR or X-ray AGN enhancement on average, except for the visually identified sample at the closest separations and those that have already coalesced into a single system. These results do not change significantly when the sample is split by X-ray luminosity.

Most studies in the nearby universe ($z \sim 0$) find significant AGN enhancement in merging and/or interacting galaxies (e.g., Alonso et al. 2007; Woods & Geller 2007; Ellison et al. 2011, 2013a, 2019; Carpineti et al. 2012; Satyapal et al. 2014; Weston et al. 2017; Fu et al. 2018). For low-redshift major galaxy pairs (stellar mass ratio < 4) at $0.01 < z < 0.20$ selected from the SDSS, Ellison et al. (2013a) find a clear trend of increasing optical AGN excess (or enhancement) with decreasing projected separation (< 40 kpc) as shown in the left panel of Figure 15. They computed the largest enhancement of a factor of $\sim$2.5 at the closest projected separation (< 10 kpc). Their estimate of the AGN enhancement for pairs with projected separation between 10 and 20 kpc is $1.95^{+0.16}_{-0.15}$, which

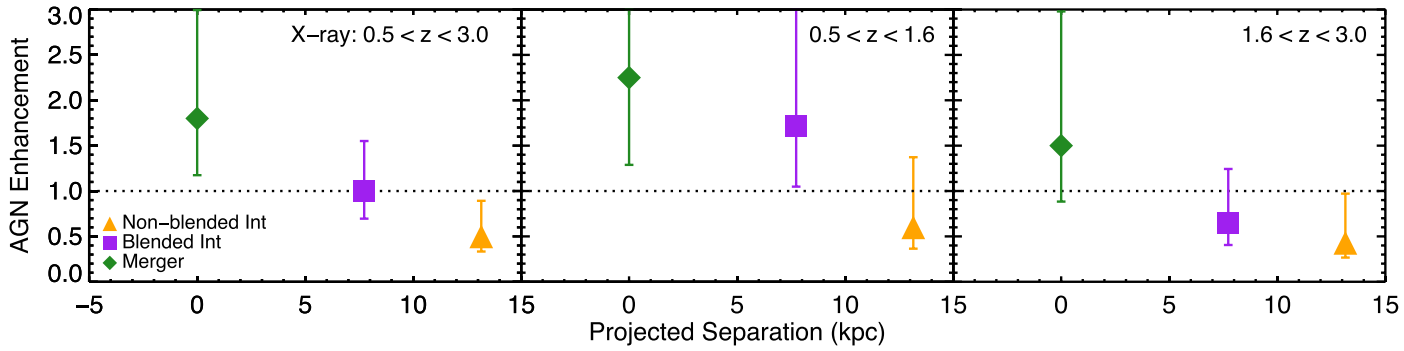

Figure 13. The level of X-ray AGN enhancement as a function of the median projected separation for our visually identified mergers (filled green diamonds), blended interactions (filled purple squares), and non-blended interactions (filled orange triangles). The left, middle, and right panels correspond to the complete ($0.5 < z < 3.0$), low-z ($0.5 < z < 1.6$), and high-z ($1.6 < z < 3.0$) samples, respectively, with their values given in Table 13. The error bars on each point reflect the 1σ binomial confidence limits, following the method of Cameron (2011). The median redshift of all three visually identified samples combined is ∼1.6.

Table 6
X-Ray AGN Enhancement for Visually Identified Mergers and Interactions: Figure 13

	Meger			Blended Int			Non-blended Int		
	z[0.5,3.0]	z[0.5,1.6]	z[1.6,3.0]	z[0.5,3.0]	z[0.5,1.6]	z[1.6,3.0]	z[0.5,3.0]	z[0.5,1.6]	z[1.6,3.0]
Galaxies	66	35	31	99	46	53	121	59	62
AGNs	6	3	3	7	4	3	4	2	2
AGN Fraction (%)	$9.1^{+4.8}_{-2.4}$	$8.6^{+7.2}_{-2.7}$	$9.7^{+7.9}_{-3.3}$	$7.1^{+3.5}_{-1.8}$	$8.7^{+6.0}_{-2.6}$	$5.6^{+4.9}_{-1.7}$	$3.3^{+2.5}_{-1.0}$	$3.4^{+4.1}_{-1.0}$	$3.2^{+4.0}_{-1.0}$
Control Galaxies	198	105	93	297	138	159	363	177	186
AGNs	10	4	6	21	7	14	24	10	14
AGN Fraction (%)	$5.1^{+2.0}_{-1.1}$	$3.8^{+2.8}_{-1.1}$	$6.5^{+3.5}_{-1.7}$	$7.1^{+1.8}_{-1.2}$	$5.1^{+2.6}_{-1.3}$	$8.8^{+2.8}_{-1.8}$	$6.6^{+1.5}_{-1.1}$	$5.6^{+2.3}_{-1.3}$	$7.5^{+2.4}_{-1.5}$
AGN Enhancement	$1.8^{+1.19}_{-0.63}$	$2.2^{+2.52}_{-0.96}$	$1.5^{+1.48}_{-0.62}$	$1.0^{+0.55}_{-0.30}$	$1.7^{+1.46}_{-0.67}$	$0.64^{+0.60}_{-0.24}$	$0.5^{+0.39}_{-0.17}$	$0.6^{+0.77}_{-0.23}$	$0.43^{+0.54}_{-0.16}$

Note. $z[a, b]$: $a <$ Redshift (z) $< b$.

Table 7
Stern et al. (2005) Identified IR AGN Enhancement for Visually Identified Mergers and Interactions: Figure 14

	Meger			Blended Int			Non-blended Int		
	z[0.5,3.0]	z[0.5,1.6]	z[1.6,3.0]	z[0.5,3.0]	z[0.5,1.6]	z[1.6,3.0]	z[0.5,3.0]	z[0.5,1.6]	z[1.6,3.0]
Galaxies	66	35	31	99	46	53	121	59	62
AGNs	12	5	7	13	5	8	22	13	9
AGN Fraction (%)	$18.18^{+5.6}_{-3.8}$	$14.3^{+7.9}_{-4.0}$	$22.6^{+9.0}_{-5.7}$	$13.1^{+4.1}_{-2.7}$	$10.9^{+6.3}_{-3.0}$	$15.1^{+6.2}_{-3.6}$	$18.2^{+4.0}_{-3.0}$	$22.0^{+6.2}_{-4.4}$	$14.5^{+5.6}_{-3.4}$
Control Galaxies	198	105	93	297	138	159	363	177	186
AGNs	34	13	21	40	11	29	55	23	32
AGN Fraction (%)	$17.2^{+3.0}_{-2.3}$	$12.4^{+3.9}_{-2.5}$	$22.6^{+4.9}_{-3.7}$	$13.5^{+2.2}_{-1.7}$	$8.0^{+2.9}_{-1.7}$	$18.2^{+3.4}_{-2.6}$	$15.1^{+2.1}_{-1.7}$	$12.99^{+2.9}_{-2.1}$	$17.2^{+3.1}_{-2.4}$
AGN Enhancement	$1.06^{+0.38}_{-0.26}$	$1.15^{+0.73}_{-0.40}$	$1.00^{+0.45}_{-0.30}$	$0.98^{+0.23}_{-0.34}$	$1.36^{+0.93}_{-0.48}$	$0.83^{+0.23}_{-0.37}$	$1.20^{+0.24}_{-0.31}$	$1.70^{+0.44}_{-0.61}$	$0.84^{+0.23}_{-0.36}$

Note. $z[a, b]$: $a <$ Redshift (z)$< b$.

is $\sim 4.9\sigma$ higher than our enhancement value for pairs ($V < 1000\,\mathrm{km\,s^{-1}}$) with projected separation between 0 and 25 kpc (median ∼14 kpc) at $0.5 < z < 3.0$. While their post-merger enhancement is higher than our value, it is almost within error bars. While the overall size of the interaction and merger samples likely plays a part in the difference between the enhancement across redshifts, the differences in how the samples were selected may also impact the results.

For the same SDSS pairs and post-merger sample as Ellison et al. (2013a), Satyapal et al. (2014) use IR observations from the Wide-field Infrared Survey Explorer (WISE) all-sky survey to estimate IR AGN enhancement as shown in the right panel of Figure 15. They identify IR AGNs using the WISE color selection criteria of Stern et al. (2012). They also find increasing IR AGN enhancement with decreasing separation at < 40 kpc, with the highest enhancement value of ∼4–6 for pairs with projected separation of less than 10 kpc. Their IR AGN enhancement for pairs with projected separation between 10 kpc and 20 kpc is $3.43^{+0.64}_{-0.63}$. It is $\sim 3.8\sigma$ higher than our IR AGN enhancement value of $1.00^{+0.58}_{-0.31}$ for pairs with projected separation between 0 and 25 kpc (median ∼14 kpc). They also estimate an enhancement of $11.2^{+3.1}_{-3.0}$ for their post-merger sample, which is $\sim 3.3\sigma$ higher than the IR AGN enhancement of $1.2^{+1.6}_{-0.5}$ for our merger sample. Their result is $\sim 2.5\sigma$ higher than the optical AGN enhancement result for the same merger sample (Ellison et al. 2013a).

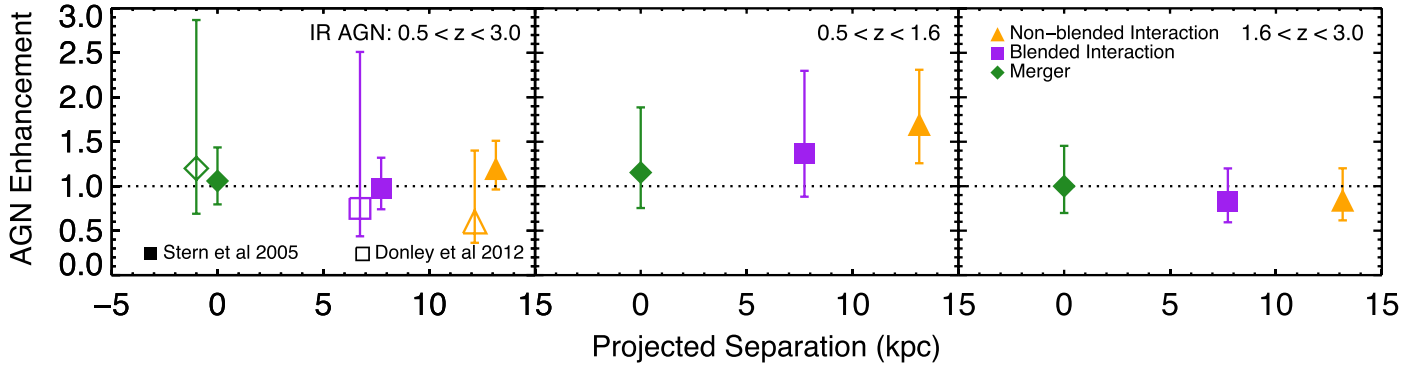

Figure 14. The level of IR AGN enhancement as a function of the median projected separation for our sample of visually identified mergers (green diamonds), blended interactions (purple squares), and non-blended interactions (orange triangles). The filled and open symbols correspond to IR AGNs identified based on Stern et al. (2005) and Donley et al. (2012) criteria, respectively. The left, middle, and right panels correspond to the complete ($0.5 < z < 3.0$), low-z ($0.5 < z < 1.6$), and high-z ($1.6 < z < 3.0$) samples, respectively, with their values given in Table 14. The error bars on each point reflect the 1σ binomial confidence limits, following the method of Cameron (2011). The median redshift of the combined samples is ∼1.6.

Table 8
IR AGN Enhancement (Donley et al. 2012 Criteria) for Visually Identified Mergers and Interactions: Left panel of Figure 14

	Merger	Blended Interaction	Non-blended Interaction
Galaxies	66	99	121
AGNs	2	1	2
AGN Fraction (%)	$3.0^{+3.7}_{-1.0}$	$1.0^{+2.2}_{-0.3}$	$1.7^{+2.1}_{-0.5}$
Control Galaxies	198	297	363
AGNs	5	4	10
AGN Fraction (%)	$2.5^{+1.6}_{-0.7}$	$1.3^{+1.0}_{-0.4}$	$2.8^{+1.1}_{-0.6}$
AGN Enhancement	$1.20^{+1.67}_{-0.51}$	$0.75^{+1.76}_{-0.31}$	$0.60^{+0.80}_{-0.23}$

Note. Merger, blended interaction and non-blended interaction are defined based on Kartaltepe et al. (2015a) (see Section 3.2).

The SDSS galaxy pair sample has a stricter relative velocity cut ($\Delta V < 300\,\mathrm{km\,s^{-1}}$) compared to our work (5000, 1000, and $500\,\mathrm{km\,s^{-1}}$). However, our results do not show a significant enhancement for the $\Delta V < 500\,\mathrm{km\,s^{-1}}$ pair sample at projected separation less than 25 kpc as shown in the left panel of Figure 9.

While in the nearby universe ∼80% of all quasars (or high-luminosity AGNs) show signs of a recent or ongoing merger (Sanders et al. 1988a, 1988b; Bennert et al. 2008; Urrutia et al. 2008), our results do not show AGN enhancement even in the highest X-ray luminosity range. Our results are consistent with the results of Marian et al. (2019), who consider the highest specific accretion broad line AGNs at the peak epoch of AGN activity around $z \sim 2$ and find no significant difference in the merger fraction of the AGN host galaxies and (mass- and redshift-matched) non-AGN galaxies. However, Treister et al. (2012) find that mergers are responsible for triggering the highest luminosity AGNs at $0 < z < 3$ ($z < 1$ for most of their sample), with no signs of redshift dependence. One possible explanation for this difference is that our work on spectroscopic pairs probes the earliest stages of the merger process, while galaxies are still distant pairs, rather than the most advanced stage mergers expected to fuel quasars, and our visually identified merger and interaction samples are too small to make a statistically significant claim.

One of the main differences between many local studies and our study is the method used to identify AGNs. Most of these local studies use optical AGNs selected using emission line ratios while we use X-ray and IR observations to identify AGNs. Since it is possible that AGNs would be visible at different wavelengths at different stages of the merger sequence, due to factors such as dust obscuration, there could be inherent differences between the level of AGN enhancement calculated based on different AGN identification methods. Furthermore, the relative timescale of AGN triggering and the merging process, as well as the duration of AGN activity, could also change with redshift, resulting in differences in AGN enhancement at high and low redshifts (McAlpine et al. 2020). However, we note that comparison between our IRAC-selected IR AGNs with WISE-selected IR AGNs among local pairs (Satyapal et al. 2014), shown in Figure 15, highlight the difference between local and high-redshift interacting systems for similar types of AGNs.

Silverman et al. (2011) present a sample of 562 galaxies in kinematic pairs ($0.25 < z < 1.05$, 1< mass ratio < 10) and find a higher (by a factor of 1.9) AGN fraction in paired galaxies at projected separations less than 75 kpc (relative line-of-sight velocity less than 500 $\mathrm{km\,s^{-1}}$) compared to their control sample of galaxies. We note that since their sample was based on zCOSMOS observations, their major (mass ratio < 4) pairs are included as a subset of the ones used for our study. However, our results are not in strong agreement.

The control sample used by Silverman et al. (2011) consists of the non-paired galaxies in their survey and the same sample is used for different separation bins. Based on K-S tests, they claim that there is no difference between the mass distribution of pairs and controls in projected separation, line-of-sight velocity, and redshift bins. Environmental effects on larger scales can also play a role in AGN fueling. Using a mock catalog of an SDSS-like survey, Perez et al. (2009) show that although mass is likely the most crucial parameter to match while generating a control sample to study the effect of galaxy interactions, by matching in both redshift and environment the differences between the pairs and control sample are reduced by 70%. Ellison et al. (2013a) find that the main reason they were able to estimate AGN excess at larger separations compared to Ellison et al. (2011) is the addition of environment-matching of controls. Hence, it is likely critical to control for environment as well. Our controls were carefully matched to each paired galaxy to account for any subtle variations in mass, redshift, and environment of the general

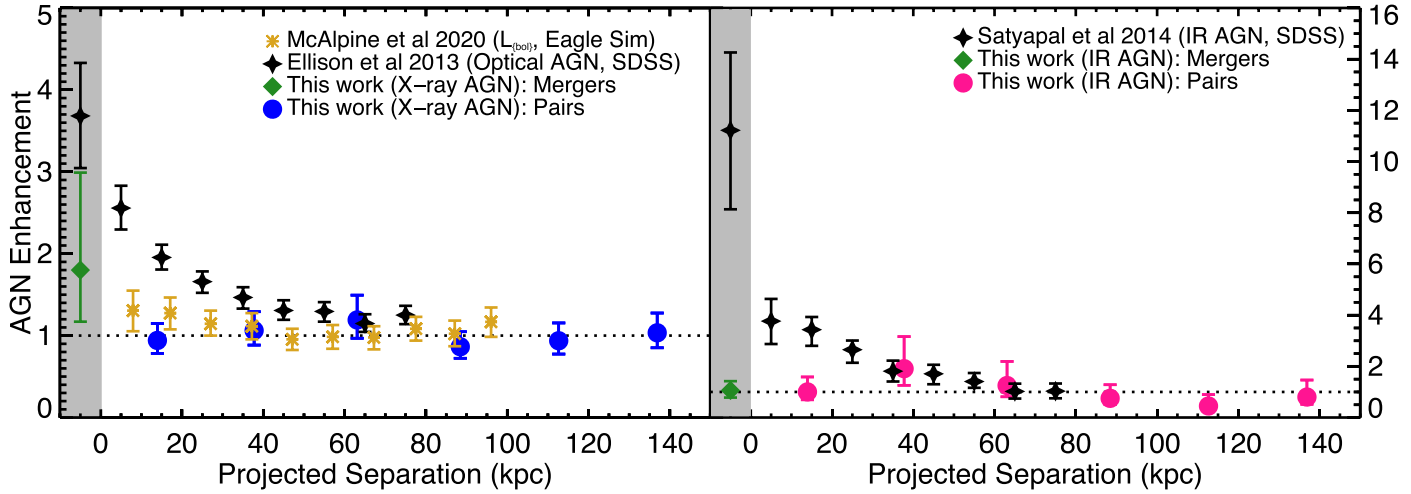

Figure 15. Comparison of our results with studies of galaxy pair samples in the local universe. Left: X-ray AGN enhancement as a function of projected separation for our sample of paired galaxies with $\Delta V < 1000$ km s^{-1} at $0.5 < z < 3.0$ (filled dark blue circles) and the visually identified merger sample (filled green diamond) in comparison with the results of Ellison et al. (2013a) for optical AGNs in SDSS spectroscopic paired galaxies and post mergers (filled black stars) at $0.01 < z < 0.20$ and the results of McAlpine et al. (2020) AGNs ($L_{\rm bol} > 2 \times 10^{42}$ erg s^{-1}) in pairs at $0.05 < z < 0.10$ from the cosmological simulation EAGLE (golden asterisks). Right: IR AGNs enhancement as a function of projected separation for our sample of paired galaxies with $\Delta V < 1000$ km s^{-1} (filled deep pink circles) and the visually identified merger sample (filled green diamond), based on the Donley et al. (2012) criteria, in comparison with the results of Satyapal et al. (2014) for IR AGNs selected from WISE in SDSS spectroscopic paired galaxies and post mergers (filled black stars). The gray shaded region in both panels corresponds to merging/post-merger systems. All spectroscopic pairs correspond to major interactions (mass ratio < 4).

galaxy population, enabled by the ever-growing set of spectroscopic observations in these fields.

Silverman et al. (2011) also include both major and minor interactions while our work focuses on just major interactions. This should affect the results, though one would expect that this would have an effect in the opposite direction to what we see (major interactions should see a stronger enhancement that minor interactions). Studies in the local universe show that the effect of minor interactions on AGN activity could be different from that of major interactions (Ellison et al. 2011). Further work at high redshift is required to determine the impact of minor mergers. We plan to explore these differences in a future paper.

We also compare our AGN enhancement results to those using the sample of kinematic pairs selected by Mantha et al. (2018) in the CANDELS fields. Applying the same cuts to their sample as we used for our pairs results in a total sample size of 154 pairs with $\Delta V < 500$ km $^{-1}$ and projected separations of 5–150 kpc. Unfortunately, there are too few pairs in the closest separation bin and too few control galaxy candidates to conduct a fair comparison with our sample. Note that this pair sample is almost an order of magnitude smaller than ours (we have 1066 pairs with $\Delta V < 500$ km $^{-1}$) because we included the larger 2 deg^2 COSMOS field, our own DEIMOS, GMOS, and MOSFIRE observations, and spectroscopic samples in these fields have generally grown since their study was first published. Since these were selected within CANDELS, the Mantha et al. (2018) pair sample is a subset of the pairs included in our analysis. This highlights the importance of using large spectroscopic samples for this analysis.

As discussed above, generating a well-matched control sample is one of the crucial parts of this analysis. Here, we highlight different factors that play a significant role in how controls are selected. One of the main limiting factors is the availability of spectroscopic redshifts. Redshift completeness falls off as a function of redshift due to the availability of spectral lines in observable wavelength ranges and the increasing faintness of galaxies at high redshift. This biases the sample toward pairs at lower redshift and the spectroscopic incompleteness results in missing pairs. An effect of this is that the control sample could contain galaxies that are actually in a pair, but we are missing the redshift for its companion. This could result in a dilution of the measured AGN enhancement, particularly at high redshift. Similarly, some galaxies in the control sample may be at an advanced merging stage and missed by our selection. We attempted to account for this by removing the visually identified mergers and interactions from the control parent sample, but since that selection was fairly conservative, there are almost certainly many mergers that have been missed and could have been included in the control sample.

It is also important to note that any biases and selection effects present in the spectroscopic redshift samples will be present in our pair sample. Spectroscopic surveys in these fields are inhomogenous overall and each survey has a different goal in mind for targeting. Of particular note, the spectroscopic completeness of X-ray AGNs is higher than the general galaxy population in these fields since there have been many campaigns to specifically target X-ray AGNs. We attempt to mitigate this by requiring all controls to have spectroscopic redshifts and all controls to come from the same field as the galaxy pairs so that any selection effects are present in both samples. Therefore, we expect that these selection effects have minimal impact on our final AGN enhancement results.

While our kinematic pair sample is not affected by the dimming of low surface brightness features at high redshift, our sample of visually identified interactions and mergers certainly are. The observational bias of surface brightness dimming results in a decrement of three magnitudes in sensitivity from $z = 0$ to $z = 1$. Despite using deep HST images to visually identify the interaction and merger samples, these samples are incomplete as many interaction features at high redshift are too faint to be identified. In addition to being difficult to identify, many classifiers may disagree on the presence of merger signatures, due to their faintness as well as to the fact that other physical processes can be responsible for morphological disturbances at high redshift. Our selection in this paper is intentionally conservative—all of the galaxies identified as

mergers and interactions have a high level of confidence due to the presence of strong signs of disturbance. Therefore, this analysis is certainly insensitive to all of the mergers in these fields and our resulting sample is very small, affecting our statistics. This could result in some missing mergers being included in our control sample, diluting any AGN enhancement in our measurement.

We compare our results for our visually identified samples with the results of Lackner et al. (2014). They apply an automated method of identifying mergers by median-filtering the high-resolution COSMOS HST images to distinguish two concentrated galaxy nuclei at small separations, i.e., to identify late-stage mergers at $0.25 < z < 1.0$, and also used X-ray observations to identify AGN. They find that their late-stage merger sample has higher X-ray AGN activity by a factor of $\sim$2 compared to their mass- and redshift-matched control sample. Our results for the visually classified merger sample are consistent within the error bars of these results.

To study the effect of using different criteria to define merger and interaction samples, we also calculate the level of AGN enhancement for a redefined sample of interacting and merging galaxies based on the criteria of Rosario et al. (2015) applied to the full visual classification catalog of Kartaltepe et al. (2015a). Rosario et al. (2015) assign an interaction metric (IM) value for each visual classification of an object. The IM value ranges from IM = 0 (a clearly undisturbed object with no obvious nearby companion) to IM = 1 (an obvious late-stage merger). The intermediate IM values of IM = 0.25 is assigned to objects in apparent pair or multiple systems (with a maximum separation of several arcseconds apart) with no clear signs of interaction, which may or may not be associated to each other, IM = 0.5 for non-blended interactions, i.e., systems with apparent interaction signs with galaxies in different *H*-band segmentation maps, and finally IM = 0.75 is assigned to blended interactions, i.e., distinct interacting galaxies that share a segmentation map. Based on the average IM (averaged over all the classification IMs), Rosario et al. (2015) define interaction classes as: $0.0 \leqslant \mathrm{IM} \leqslant 0.2$ for Isolated, $0.2 < \mathrm{IM} \leqslant 0.5$ for interacting, and $0.5 < \mathrm{IM} \leqslant 1.0$ for mergers. Therefore, everything with a visual classification is divided into these three classes. These classes are more liberally defined than our constraints. For example, if we have a galaxy for which each classifier agrees about its classification as a "blended interaction," it would be included in the "merger" (not interaction) class of the Rosario et al. (2015) classification metric.

Applying this metric to the Kartaltepe et al. (2015a) catalog in all five CANDELS fields, and applying our mass and redshift cuts, we identified 518 mergers, 2120 interactions, and 4606 isolated galaxies. We match control galaxies for these objects using photometric redshifts (following the same method that is used for our visually identified interaction and merger samples). We calculate an X-ray AGN enhancement of $1.07^{+0.22}_{-0.17}$ and $0.80^{+0.08}_{-0.07}$ for their merger and interaction samples, respectively. While the error bars are smaller due to the larger sample identified this way, the result agrees overall with our sample discussed above. Hence, we do not find significant AGN enhancement in this more inclusive merger and interaction sample.

Another approach to understanding the effect of galaxy interactions on AGN activity is to use simulations of galaxy mergers. Most simulations of galaxy mergers between nearby massive gas-rich galaxies show enhancement in both AGN activity and star formation rate caused by interaction-induced gravitational torques (e.g., Barnes & Hernquist 1991; Mihos & Hernquist 1996; Hopkins et al. 2009). However, for high-redshift galaxy interactions and mergers, simulations find a varying range of results.

McAlpine et al. (2020) conducted a study over a large redshift range that uses a similar approach to ours using the cosmological hydrodynamical EAGLE simulation. They find a higher AGN fraction in galaxies with close major companions relative to their controls. As shown in the left panel of Figure 15, for AGNs identified based on a bolometric luminosity cut ($L_{\mathrm{bol}} > 10^{42}$ erg s^{-1}), they see an enhancement of $1.28^{+0.23}_{-0.21}$ at projected separation of $\sim$15 kpc at $0.05 < z < 0.10$, which is within the error bars of our X-ray AGN enhancement value ($0.94^{+0.21}_{-0.16}$) for projected separation < 25 kpc at $0.5 < z < 3.0$. However, for AGNs defined based on an Eddington rate cut, they see a strong trend of increasing AGN excess with decreasing projected separation starting at 3D separations of 50–100 kpc for $z < 2$ galaxies with the highest excess value of 1.2–1.3 at 10 kpc. They defined redshift bins of $0 < z < 1$, $1 < z < 2$, $2 < z < 5$, and find a decreasing AGN enhancement with increasing redshift. For $z > 1$ for both AGN definitions, they find excess values oscillating around 1.2–1.3.

McAlpine et al. (2020) also show the effect of different ways of selecting controls matched to a range of different parameters and their combinations: mass, redshift, environment, gas mass, BH mass, and halo mass. They find that the AGN excess value decreases when the number of matched parameters increases with a deviation within a factor of two. Furthermore, they find that results based on the Eddington luminosity criteria were more sensitive to the control matching compared to the results based on the bolometric luminosity criteria. They also find that the trend of increment in AGN excess with decreasing separation is not affected by the change in the matching criteria.

We control for mass, redshift, and environment, and our results do not show any significant AGN enhancement for the paired galaxies. For the visually identified sample there are hints of slight X-ray (Figure 13) and IR AGNs (Figure 14) enhancement at $0.5 < z < 1.6$ with very low ($<1.5\sigma$) statistical significance. These results suggest that there might be redshift evolution in the effect of interactions and mergers on AGN activity, even at $z < 1$. As suggested by simulations, the interaction and merger induced gas inflows responsible for the enhancement in AGN activity could strongly depend on the properties of the galaxies, such as their gas fractions (Cox et al. 2008; Di Matteo et al. 2008; Fensch et al. 2017). The gas fraction in massive spiral galaxies increases from $\sim$10% at low redshift ($z \sim 0$) to $\sim$50% at high redshift (z $\sim$2, Daddi et al. 2010; Tacconi et al. 2010; Scoville et al. 2014). Furthermore, gravitational instabilities, and hence velocity dispersion, are also higher ($\sigma \sim 40$ km s^{-1}) at high redshift compared to low redshift ($\sigma \sim 10$ km s^{-1}) (Stott et al. 2016). This may weaken the strong inflows, essential for the enhancement in AGN activity. The efficiency of galaxy interactions and mergers in enhancing the AGN activity could thus be weaker at high redshift compared to low redshift.

6. Summary

In this paper, we investigate the effect of galaxy interactions on AGN activity using deep multiwavelength observations

from the CANDELS and COSMOS surveys. We generated the largest known sample of 2381 major spectroscopic galaxy pairs with $\Delta V < 5000\,\mathrm{km\,s^{-1}}$ over $0.5 < z < 3.0$, with the stellar mass of both galaxies greater than $10^{10}\,M_{\odot}$ and with the stellar mass ratio of the primary (more massive) to the secondary (less massive) galaxy less than four. We also selected samples of visually identified interactions and mergers consisting of 61 galaxy pairs of non-blended interactions, 100 galaxy pairs of blended interactions, and 66 galaxy mergers.

To compute the interaction-induced AGN enhancement, we generate a stellar mass-, redshift-, and environment-matched control sample of three galaxies for each paired galaxy and visually identified interaction and merger selected from the same field. We define the AGN enhancement as the ratio of the AGN fraction of the paired or visually identified galaxy samples to that of the corresponding control galaxy sample.

We explored the effect of using different relative line-of-sight velocity cuts by constructing samples with three different cuts: $\Delta V < 500\,\mathrm{km\,s^{-1}}$ (1066 pairs), $\Delta V < 1000\,\mathrm{km\,s^{-1}}$ (1345 pairs), and $\Delta V < 5000\,\mathrm{km\,s^{-1}}$ (2381 pairs). We do not see significant AGN enhancement for any of these samples; the results of all three are consistent within error bars.

For the closest projected separation bin (< 25 kpc, median ∼14 kpc) in our sample ($0.5 < z < 3.0$, $\Delta V < 1000\,\mathrm{km\,s^{-1}}$), we find enhancements of a factor of $0.94^{+0.21}_{-0.16}$ and $1.00^{+0.58}_{-0.31}$ for X-ray and IR-selected AGNs, respectively. These results appear to be somewhat in contrast with $z \sim 0$ results that indicate strong AGN enhancement in the closest pairs, as shown in Figure 15. At roughly equivalent small separations (∼15 kpc), our X-ray enhancement result is $\sim 4.9\sigma$ lower than the local optical AGN enhancement Ellison et al. (2013a), and our IR AGN enhancement is $\sim 3.8\sigma$ lower than local IR AGN enhancement (Satyapal et al. 2014). While the X-ray and optical AGN enhancement results for merger samples are almost within error bars, our IR AGN enhancement is ∼3.3 sigma lower than the local result. These discrepancies suggest that high-redshift mergers and interactions might be less efficient at triggering AGNs compared to such interactions at low redshift as also suggested by some simulations (e.g., Fensch et al. 2017; McAlpine et al. 2020).

Considering the different depth of X-ray observations in the CANDELS and COSMOS fields, we also apply different redshift and luminosity cuts to account for X-ray completeness and to conduct a consistent analysis among all the fields. We further divide our sample at its median redshift of ∼1.0 to compare the enhancement results in the low-redshift ($0.5 < z < 1.0$) and high-redshift ($1.0 < z < 3.0$) halves of the sample. We find no significant enhancement in AGN activity in any of our pair separation, redshift, or X-ray luminosity bins in our galaxy pairs and visually identified mergers relative to the control sample of galaxies.

The error bars on our results are large enough to hide possible low-level AGN enhancement. A larger sample of pairs across a wide range in redshift is needed, especially at smaller separations, to make statistically significant claims about AGN enhancement level differences at high and low redshifts. In the upcoming decade, surveys using facilities such as the James Webb Space Telescope, the Vera Rubin Observatory, Euclid, and the Nancy Grace Roman Space Telescope, along with follow-up spectroscopic and multiwavelength broadband observations (e.g., X-ray observations from eROSITA) will help to improve the statistics and enable a quantitative determination of how galaxy interactions and mergers affect AGN activity over cosmic time.

We thank the anonymous reviewer for their critical reading of the manuscript and for providing detailed and insightful comments, which greatly enhanced the quality and clarity of the paper. Support for this work was provided by NASA through grants HST-GO-13657.010-A and HST-AR-14298.004-A awarded by the Space Telescope Science Institute, which is operated by the Association of Universities for Research in Astronomy, Inc., under NASA contract NAS 5-26555. Support was also provided by NASA through grant NNX16AB36G as part of the Astrophysics Data Analysis Program. This work was also supported by start-up funds and the Dean's Research Initiation Grant fund from the Rochester Institute of Technology's College of Science. Spectral energy distribution fitting was performed using the computational resources and support from Research Computing Services at the Rochester Institute of Technology (Rochester Institute of Technology 2019). E.S. thanks the LSSTC Data Science Fellowship Program, which is funded by LSSTC, NSF Cybertraining Grant #1829740, the Brinson Foundation, and the Moore Foundation; her participation in the program has benefited this work. H.I. acknowledges support from JSPS KAKENHI Grant No. JP19K23462. E.T. acknowledges support from FONDECYT Regular 1190818, ANID PIA ACT172033 and Basal-CATA AFB170002.

Some of the data presented herein were obtained at the W. M. Keck Observatory, which is operated as a scientific partnership among the California Institute of Technology, the University of California and the National Aeronautics and Space Administration. The Observatory was made possible by the generous financial support of the W. M. Keck Foundation. Based in part on observations obtained at the international Gemini Observatory and processed using the Gemini IRAF package (Tody & Crawford 1986; Tody 1993), a program of NOIRLab, which is managed by the Association of Universities for Research in Astronomy (AURA) under a cooperative agreement with the National Science Foundation. on behalf of the Gemini Observatory partnership: the National Science Foundation (United States), National Research Council (Canada), Agencia Nacional de Investigación y Desarrollo (Chile), Ministerio de Ciencia, Tecnología e Innovación (Argentina), Ministério da Ciência, Tecnologia, Inovações e Comunicações (Brazil), and Korea Astronomy and Space Science Institute (Republic of Korea). The authors wish to recognize and acknowledge the very significant cultural role and reverence that the summit of Maunakea has always had within the indigenous Hawaiian community. We are most fortunate to have the opportunity to conduct observations from this mountain.

This work is also based in part on observations made with the NASA/ESA Hubble Space Telescope, obtained from the Data Archive at the Space Telescope Science Institute, which is operated by the Association of Universities for Research in Astronomy, Inc., under NASA contract NAS 5-26555, observations made with the Spitzer Space Telescope, which is operated by the Jet Propulsion Laboratory, California Institute of Technology under a contract with NASA, and observations made by the Chandra X-ray Observatory and published previously in cited articles.

Software: LePhare (Arnouts et al. 2002; Ilbert et al. 2006), MAGPHYS (da Cunha et al. 2008), SpecPro (Masters & Capak 2011), spec2d IDL pipeline (Cooper et al. 2012b; Newman et al. 2013), IRAF (Tody & Crawford 1986; Tody 1993).

ORCID iDs

Ekta A. Shah https://orcid.org/0000-0001-7811-9042
Jeyhan S. Kartaltepe https://orcid.org/0000-0001-9187-3605
Antonello Calabro https://orcid.org/0000-0003-2536-1614
Nima Chartab https://orcid.org/0000-0003-3691-937X
Christopher J. Conselice https://orcid.org/0000-0003-1949-7638
Darren J. Croton https://orcid.org/0000-0002-5009-512X
Jennifer Donley https://orcid.org/0000-0002-6589-2017
Alexander de la Vega https://orcid.org/0000-0002-6219-5558
Nimish P. Hathi https://orcid.org/0000-0001-6145-5090
Olivier Ilbert https://orcid.org/0000-0002-7303-4397
Hanae Inami https://orcid.org/0000-0003-4268-0393
Anton M. Koekemoer https://orcid.org/0000-0002-6610-2048
Brian C. Lemaux https://orcid.org/0000-0002-1428-7036
Stefano Marchesi https://orcid.org/0000-0001-5544-0749
Marie Martig https://orcid.org/0000-0001-5454-1492
Daniel C. Masters https://orcid.org/0000-0001-5382-6138
Jorge Moreno https://orcid.org/0000-0002-3430-3232
Hooshang Nayyeri https://orcid.org/0000-0001-8242-9983
Mara Salvato https://orcid.org/0000-0001-7116-9303
Gregory F. Snyder https://orcid.org/0000-0002-4226-304X
Amber N. Straughn https://orcid.org/0000-0002-4772-7878
Ezequiel Treister https://orcid.org/0000-0001-7568-6412

References

Alexander, D. M., Bauer, F. E., Brandt, W. N., et al. 2003, AJ, 126, 539
Alonso, M. S., Lambas, D. G., Tissera, P., & Coldwell, G. 2007, MNRAS, 375, 1017
Alonso-Herrero, A., Pérez-González, P. G., Alexander, D. M., et al. 2006, ApJ, 640, 167
Arnouts, S., Le Floc'h, E., Chevallard, J., et al. 2013, A&A, 558, A67
Arnouts, S., Moscardini, L., Vanzella, E., et al. 2002, MNRAS, 329, 355
Ashby, M. L. N., Willner, S. P., Fazio, G. G., et al. 2013, ApJ, 769, 80
Ashby, M. L. N., Willner, S. P., Fazio, G. G., et al. 2015, ApJS, 218, 33
Balestra, I., Mainieri, V., Popesso, P., et al. 2010, A&A, 512, A12
Barger, A. J., Cowie, L. L., & Wang, W.-H. 2008, ApJ, 689, 687
Barmby, P., Huang, J.-S., Ashby, M. L. N., et al. 2008, ApJS, 177, 431
Barnes, J. E., & Hernquist, L. E. 1991, ApJL, 370, L65
Barro, G., Pérez-González, P. G., Cava, A., et al. 2019, ApJS, 243, 22
Bennert, N., Canalizo, G., Jungwiert, B., et al. 2008, ApJ, 677, 846
Bertin, E., & Arnouts, S. 1996, A&AS, 117, 393
Bradshaw, E. J., Almaini, O., Hartley, W. G., et al. 2013, MNRAS, 433, 194
Bruzual, G., & Charlot, S. 2003, MNRAS, 344, 1000
Calzetti, D., Armus, L., Bohlin, R. C., et al. 2000, ApJ, 533, 682
Cameron, E. 2011, PASA, 28, 128
Capak, P., Cowie, L. L., Hu, E. M., et al. 2004, AJ, 127, 180
Carpineti, A., Kaviraj, S., Darg, D., et al. 2012, MNRAS, 420, 2139
Chabrier, G. 2003, PASP, 115, 763
Civano, F., Marchesi, S., Comastri, A., et al. 2016, ApJ, 819, 62
Coil, A. L., Blanton, M. R., Burles, S. M., et al. 2011, ApJ, 741, 8
Coil, A. L., Davis, M., Madgwick, D. S., et al. 2004, ApJ, 609, 525
Comparat, J., Richard, J., Kneib, J.-P., et al. 2015, A&A, 575, A40
Cooper, M. C., Aird, J. A., Coil, A. L., et al. 2011, ApJS, 193, 14
Cooper, M. C., Griffith, R. L., Newman, J. A., et al. 2012a, MNRAS, 419, 3018
Cooper, M. C., Newman, J. A., Davis, M., Finkbeiner, D. P., & Gerke, B. F. 2012b, spec2d: DEEP2 DEIMOS Spectral Pipeline, Astrophysics Source Code Library version 1.1.4, ascl:1203.003
Cooper, M. C., Yan, R., Dickinson, M., et al. 2012c, MNRAS, 425, 2116
Cowie, L. L., Barger, A. J., Hu, E. M., Capak, P., & Songaila, A. 2004, AJ, 127, 3137
Cox, T. J., Jonsson, P., Somerville, R. S., Primack, J. R., & Dekel, A. 2008, MNRAS, 384, 386
Croom, S. M., Warren, S. J., & Glazebrook, K. 2001, MNRAS, 328, 150
da Cunha, E., Charlot, S., & Elbaz, D. 2008, MNRAS, 388, 1595
Daddi, E., Cimatti, A., Renzini, A., et al. 2004, ApJL, 600, L127
Daddi, E., Elbaz, D., Walter, F., et al. 2010, ApJL, 714, L118
Dahlen, T., Mobasher, B., Faber, S. M., et al. 2013, ApJ, 775, 93
Damjanov, I., Zahid, H. J., Geller, M. J., Fabricant, D. G., & Hwang, H. S. 2018, ApJS, 234, 21
Darg, D. W., Kaviraj, S., Lintott, C. J., et al. 2010, MNRAS, 401, 1552
Darvish, B., Mobasher, B., Sobral, D., Scoville, N., & Aragon-Calvo, M. 2015, ApJ, 805, 121
Davis, M., Guhathakurta, P., Konidaris, N. P., et al. 2007, ApJL, 660, L1
Di Matteo, P., Bournaud, F., Martig, M., et al. 2008, A&A, 492, 31
Dickinson, M., Giavalisco, M. & GOODS Team 2003, in The Mass of Galaxies at Low and High Redshift, ed. R. Bender & A. Renzini (Berlin: Springer), 324
Donley, J. L., Kartaltepe, J., Kocevski, D., et al. 2018, ApJ, 853, 63
Donley, J. L., Koekemoer, A. M., Brusa, M., et al. 2012, ApJ, 748, 142
Ellison, S. L., Mendel, J. T., Patton, D. R., & Scudder, J. M. 2013a, MNRAS, 435, 3627
Ellison, S. L., Mendel, J. T., Scudder, J. M., Patton, D. R., & Palmer, M. J. D. 2013b, MNRAS, 430, 3128
Ellison, S. L., Patton, D. R., Mendel, J. T., & Scudder, J. M. 2011, MNRAS, 418, 2043
Ellison, S. L., Patton, D. R., Simard, L., et al. 2010, MNRAS, 407, 1514
Ellison, S. L., Patton, D. R., Simard, L., & McConnachie, A. W. 2008, AJ, 135, 1877
Ellison, S. L., Viswanathan, A., Patton, D. R., et al. 2019, MNRAS, 487, 2491
Elvis, M., Civano, F., Vignali, C., et al. 2009, ApJS, 184, 158
Faber, S. M., Phillips, A. C., Kibrick, R. I., et al. 2003, Proc. SPIE, 4841, 1657
Fensch, J., Renaud, F., Bournaud, F., et al. 2017, MNRAS, 465, 1934
Ferrarese, L., & Merritt, D. 2000, ApJL, 539, L9
Ferreras, I., Pasquali, A., Malhotra, S., et al. 2009, ApJ, 706, 158
Fitzpatrick, E. L., & Massa, D. 1986, ApJ, 307, 286
Fu, H., Steffen, J. L., Gross, A. C., et al. 2018, ApJ, 856, 93
Galametz, A., Grazian, A., Fontana, A., et al. 2013, ApJS, 206, 10
Gebhardt, K., Bender, R., Bower, G., et al. 2000, ApJL, 539, L13
Giavalisco, M., Ferguson, H. C., Koekemoer, A. M., et al. 2004, ApJL, 600, L93
Grogin, N. A., Conselice, C. J., Chatzichristou, E., et al. 2005, ApJL, 627, L97
Grogin, N. A., Kocevski, D. D., Faber, S. M., et al. 2011, ApJS, 197, 35
Guo, Y., Ferguson, H. C., Giavalisco, M., et al. 2013, ApJS, 207, 24
Hasinger, G., Capak, P., Salvato, M., et al. 2018, ApJ, 858, 77
Hewlett, T., Villforth, C., Wild, V., et al. 2017, MNRAS, 470, 755
Hopkins, P. F., Cox, T. J., Younger, J. D., & Hernquist, L. 2009, ApJ, 691, 1168
Ilbert, O., Arnouts, S., McCracken, H. J., et al. 2006, A&A, 457, 841
Ilbert, O., Capak, P., Salvato, M., et al. 2009, ApJ, 690, 1236
Inami, H., Bacon, R., Brinchmann, J., et al. 2017, A&A, 608, A2
Kartaltepe, J. S., Mozena, M., Kocevski, D., et al. 2015a, ApJS, 221, 11
Kartaltepe, J. S., Sanders, D. B., Le Floc'h, E., et al. 2010, ApJ, 721, 98
Kartaltepe, J. S., Sanders, D. B., Silverman, J. D., et al. 2015b, ApJL, 806, L35
Kocevski, D. D., Brightman, M., Nandra, K., et al. 2015, ApJ, 814, 104
Kocevski, D. D., Faber, S. M., Mozena, M., et al. 2012, ApJ, 744, 148
Kocevski, D. D., Hasinger, G., Brightman, M., et al. 2018, ApJS, 236, 48
Koekemoer, A. M., Aussel, H., Calzetti, D., et al. 2007, ApJS, 172, 196
Koekemoer, A. M., Faber, S. M., Ferguson, H. C., et al. 2011, ApJS, 197, 36
Koss, M., Mushotzky, R., Veilleux, S., & Winter, L. 2010, ApJL, 716, L125
Kriek, M., Shapley, A. E., Reddy, N. A., et al. 2015, ApJS, 218, 15
Krogager, J.-K., Zirm, A. W., Toft, S., Man, A., & Brammer, G. 2014, ApJ, 797, 17
Kurk, J., Cimatti, A., Daddi, E., et al. 2013, A&A, 549, A63
Lackner, C. N., Silverman, J. D., Salvato, M., et al. 2014, AJ, 148, 137
Laidler, V. G., Papovich, C., Grogin, N. A., et al. 2007, PASP, 119, 1325
Laigle, C., McCracken, H. J., Ilbert, O., et al. 2016, ApJS, 224, 24
Laird, E. S., Nandra, K., Georgakakis, A., et al. 2009, ApJS, 180, 102
Lawrence, A., Warren, S. J., Almaini, O., et al. 2007, MNRAS, 379, 1599
Le Fèvre, O., Cassata, P., Cucciati, O., et al. 2013, A&A, 559, A14
Le Fèvre, O., Tasca, L. A. M., Cassata, P., et al. 2015, A&A, 576, A79
Le Fèvre, O., Vettolani, G., Paltani, S., et al. 2004, A&A, 428, 1043
Lee, K.-S., Ferguson, H. C., Wiklind, T., et al. 2012, ApJ, 752, 66
Lemaux, B. C., Tomczak, A. R., Lubin, L. M., et al. 2017, MNRAS, 472, 419
Lilly, S. J., Le Brun, V., Maier, C., et al. 2009, ApJS, 184, 218
Lilly, S. J., Le Fèvre, O., Renzini, A., et al. 2007, ApJS, 172, 70
Lotz, J. M., Jonsson, P., Cox, T. J., & Primack, J. R. 2008, MNRAS, 391, 1137
Mantha, K. B., McIntosh, D. H., Brennan, R., et al. 2018, MNRAS, 475, 1549
Marchesi, S., Civano, F., Elvis, M., et al. 2016, ApJ, 817, 34
Marian, V., Jahnke, K., Mechtley, M., et al. 2019, ApJ, 882, 141
Masters, D., & Capak, P. 2011, PASP, 123, 638
Masters, D. C., Stern, D. K., Cohen, J. G., et al. 2019, ApJ, 877, 81

McAlpine, S., Harrison, C. M., Rosario, D. J., et al. 2020, MNRAS, 494, 5713
McConnell, N. J., Ma, C.-P., Murphy, J. D., et al. 2012, ApJ, 756, 179
McLure, R. J., Pentericci, L., Cimatti, A., et al. 2018, MNRAS, 479, 25
Mignoli, M., Cimatti, A., Zamorani, G., et al. 2005, A&A, 437, 883
Mihos, J. C., & Hernquist, L. 1996, ApJ, 464, 641
Mobasher, B., Dahlen, T., Ferguson, H. C., et al. 2015, ApJ, 808, 101
Momcheva, I. G., Brammer, G. B., van Dokkum, P. G., et al. 2016, ApJS, 225, 27
Moran, E. C., Lehnert, M. D., & Helfand, D. J. 1999, ApJ, 526, 649
Morris, A. M., Kocevski, D. D., Trump, J. R., et al. 2015, AJ, 149, 178
Nandra, K., Laird, E. S., Aird, J. A., et al. 2015, ApJS, 220, 10
Nayyeri, H., Hemmati, S., Mobasher, B., et al. 2017, ApJS, 228, 7
Newman, J. A., Cooper, M. C., Davis, M., et al. 2013, ApJS, 208, 5
Onodera, M., Renzini, A., Carollo, M., et al. 2012, ApJ, 755, 26
Patton, D. R., Ellison, S. L., Simard, L., McConnachie, A. W., & Mendel, J. T. 2011, MNRAS, 412, 591
Patton, D. R., Torrey, P., Ellison, S. L., Mendel, J. T., & Scudder, J. M. 2013, MNRAS, 433, L59
Pentericci, L., Vanzella, E., Castellano, M., et al. 2018, A&A, 619, A147
Perez, J., Tissera, P., & Blaizot, J. 2009, MNRAS, 397, 748
Popesso, P., Dickinson, M., Nonino, M., et al. 2009, A&A, 494, 443
Prevot, M. L., Lequeux, J., Prevot, L., Maurice, E., & Rocca-Volmerange, B. 1984, A&A, 132, 389
Ravikumar, C. D., Puech, M., Flores, H., et al. 2007, A&A, 465, 1099
Reddy, N. A., Steidel, C. C., Erb, D. K., Shapley, A. E., & Pettini, M. 2006, ApJ, 653, 1004
Roche, N. D., Dunlop, J., Caputi, K. I., et al. 2006, MNRAS, 370, 74
Rochester Institute of Technology 2019, Research Computing Services, Rochester Institute of Technology, doi:10.34788/0S3G-QD15, https://www.rit.edu/researchcomputing/
Rogers, B., Ferreras, I., Kaviraj, S., Pasquali, A., & Sarzi, M. 2009, MNRAS, 399, 2172
Rosario, D. J., McIntosh, D. H., van der Wel, A., et al. 2015, A&A, 573, A85
Sanders, D. B., Salvato, M., Aussel, H., et al. 2007, ApJS, 172, 86
Sanders, D. B., Soifer, B. T., Elias, J. H., et al. 1988a, ApJ, 325, 74
Sanders, D. B., Soifer, B. T., Elias, J. H., Neugebauer, G., & Matthews, K. 1988b, ApJL, 328, L35
Santini, P., Ferguson, H. C., Fontana, A., et al. 2015, ApJ, 801, 97
Satyapal, S., Ellison, S. L., McAlpine, W., et al. 2014, MNRAS, 441, 1297
Schawinski, K., Simmons, B. D., Urry, C. M., Treister, E., & Glikman, E. 2012, MNRAS, 425, L61
Schawinski, K., Treister, E., Urry, C. M., et al. 2011, ApJL, 727, L31
Scodeggio, M., Guzzo, L., Garilli, B., et al. 2018, A&A, 609, A84
Scoville, N., Aussel, H., Brusa, M., et al. 2007, ApJS, 172, 1
Scoville, N., Aussel, H., Sheth, K., et al. 2014, ApJ, 783, 84
Scudder, J. M., Ellison, S. L., Torrey, P., Patton, D. R., & Mendel, J. T. 2012, MNRAS, 426, 549
Silverman, J. D., Kampczyk, P., Jahnke, K., et al. 2011, ApJ, 743, 2
Silverman, J. D., Kashino, D., Sanders, D., et al. 2015, ApJS, 220, 12
Silverman, J. D., Mainieri, V., Salvato, M., et al. 2010, ApJS, 191, 124
Stefanon, M., Yan, H., Mobasher, B., et al. 2017, ApJS, 229, 32
Stern, D., Assef, R. J., Benford, D. J., et al. 2012, ApJ, 753, 30
Stern, D., Eisenhardt, P., Gorjian, V., et al. 2005, ApJ, 631, 163
Stott, J. P., Swinbank, A. M., Johnson, H. L., et al. 2016, MNRAS, 457, 1888
Straatman, C. M. S., van der Wel, A., Bezanson, R., et al. 2018, ApJS, 239, 27
Szokoly, G. P., Bergeron, J., Hasinger, G., et al. 2004, ApJS, 155, 271
Tacconi, L. J., Genzel, R., Neri, R., et al. 2010, Natur, 463, 781
Tasca, L. A. M., Le Fèvre, O., Hathi, N. P., et al. 2015, A&A, 581, A54
Tody, D. 1986, Proc. SPIE, 627, 733
Tody, D. 1993, in ASP Conf. Ser. 52, Astronomical Data Analysis Software and Systems II, ed. R. J. Hanisch, R. J. V. Brissenden, & J. Barnes (San Francisco, CA: ASP), 173
Tomczak, A. R., Lemaux, B. C., Lubin, L. M., et al. 2017, MNRAS, 472, 3512
Treister, E., Schawinski, K., Urry, C. M., & Simmons, B. D. 2012, ApJL, 758, L39
Trump, J. R., Impey, C. D., Elvis, M., et al. 2009, ApJ, 696, 1195
Urrutia, T., Lacy, M., & Becker, R. H. 2008, ApJ, 674, 80
Urrutia, T., Wisotzki, L., Kerutt, J., et al. 2019, A&A, 624, A141
van der Wel, A., Franx, M., van Dokkum, P. G., & Rix, H. W. 2004, ApJL, 601, L5
van der Wel, A., Noeske, K., Bezanson, R., et al. 2016, ApJS, 223, 29
Vanzella, E., Cristiani, S., Dickinson, M., et al. 2008, A&A, 478, 83
Vanzella, E., Giavalisco, M., Dickinson, M., et al. 2009, ApJ, 695, 1163
Villforth, C., Hamilton, T., Pawlik, M. M., et al. 2017, MNRAS, 466, 812
Weston, M. E., McIntosh, D. H., Brodwin, M., et al. 2017, MNRAS, 464, 3882
Wirth, G. D., Trump, J. R., Barro, G., et al. 2015, AJ, 150, 153
Wirth, G. D., Willmer, C. N. A., Amico, P., et al. 2004, AJ, 127, 3121
Woods, D. F., & Geller, M. J. 2007, AJ, 134, 527
Xue, Y. Q., Luo, B., Brandt, W. N., et al. 2011, ApJS, 195, 10
Yoshikawa, T., Akiyama, M., Kajisawa, M., et al. 2010, ApJ, 718, 112